Molecular Catalysis 578 (2025) 114997

Contents lists available at ScienceDirect

Molecular Catalysis

journal homepage: www.journals.elsevier.com/molecular-catalysis

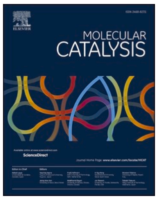

Research Paper

Environmentally friendly and recyclable Dawson-type polyoxometalate: A novel homogeneous catalytic system for degradation of dye pollutants

Mohammed Grabsi [a,*], Nacéra Zabat [a], Mohamed Djermane [b], Abdeltif Amrane [c]

[a] Department of Process Engineering, Faculty of Engineering, Badji Mokhtar Annaba University, P.O. Box 12, 23000 Annaba, Algeria
[b] Laboratory of Physics of Matter and Radiation, Department of Process Engineering, Faculty of Sciences and Technology, Mohamed Cherif Messadia – Souk Ahras University, P.O. Box: 1553, 41000 Souk Ahras, Algeria
[c] Ecole Nationale Supérieure de Chimie de Rennes, University of Rennes, CNRS, ISCR-UMR6226, 35000 Rennes, France

ARTICLE INFO

Keywords:
Homogenous catalysis
Dawson polyoxometalate
Recyclable catalyst
Oxidation process
Dye degradation
Water treatment

ABSTRACT

This research paper investigates the catalytic potential of a Dawson-type polyoxometalate-based metal complex (Co-POM) in the efficient degradation of Indigo Carmine (IC) and Methyl Orange (MO) dyes. The synthesized complex was characterized using a variety of characterization techniques, and its catalytic activity was evaluated during the degradation of these dyes under different experimental conditions. The results of the study reveal that this new environmental homogeneous catalytic system (H_2O_2/Co-POM/Dye) exhibits notable catalytic efficiency, leading to effective degradation of the dyes under consideration. The influence of various parameters on catalytic performance was systematically investigated.The cobalt-substituted complex (Co-POM) showed the best catalytic efficiency compared with other transition metal-substituted POMs {Ni(II), Cu(II), Mo(II)} and the parent POM, with a degradation of 87.4 % for IC and 94.3% for MO under the following optimized conditions: an initial hydrogen peroxide (H_2O_2) concentration of 0.02 M, a catalyst concentration of 0.2 mM, and an initial dye concentration of 5 mg/L at pH 3 and room temperature (25 °C). It revealed the oxidative role of hydroxyl radicals ($OH^{\bullet}$), hydroperoxyl radicals ($HO_2^{\bullet}$), and superoxydes ($O_2{\bullet}$) as reactive species, on the basis of which a plausible degradation mechanism is proposed.The recyclability test indicated good catalyst stability over five consecutive cycles with a very low loss of catalytic efficiency (~5 %). Their stability and robustness were verified by various characterization techniques such as UV–vis spectroscopy, FT-IR spectroscopy, single crystal X-ray Diffraction (XRD), Field Emission Scanning Electron Microscopy (FE-SEM), and Energy Dispersive X-ray analysis (EDX).

1. Introduction

Industrial activities produce significant quantities of wastewater, often contaminated by polluting organic and mineral substances [1,2]. Synthetic dyes are among the organic contaminants that play a major role in today's industry [3,4]. They are frequently used in various industrial sectors such as the paper industry [5], cosmetics [6], pharmaceuticals [7], agri-food [8] and more particularly in the textile industry [9]. These non-degradable dyes can cause various alterations and have the potential to pollute the environment and harm health in the short to medium term [10].

To maintain and improve the quality of these resources, various conventional treatment techniques have been applied, including adsorption on various solid supports [11,12], chemical oxidation [13], coagulation-flocculation [14], biological processes via biocomposite [15,16], and synergistic processes [17–19].

It is essential to look for more appropriate treatment techniques that are both economical and effective, in order to purify effluents before they are discharged into the environment, or to rehabilitate sources to obtain safe drinking water.

A great deal of research has been carried out in recent years to develop new treatment methods [20]. Among the various methods available, advanced oxidation processes stand out as very promising approaches to the degradation of organic pollutants [21].

Their operation is based on the total oxidation reaction of the constituent elements of aqueous pollutants, converting them into carbon dioxide (CO_2), water (H_2O) and inorganic residues that can be retained by filtration [22].

Oxidative treatment techniques can be classified into four distinct categories: (a) homogeneous-phase chemical oxidation processes [23];

---

* Corresponding author.
E-mail addresses: mohammed.grabsi@gmail.com, mohamed.grabsi@univ-annaba.org (M. Grabsi).

https://doi.org/10.1016/j.mcat.2025.114997
Received 4 November 2024; Received in revised form 1 March 2025; Accepted 4 March 2025

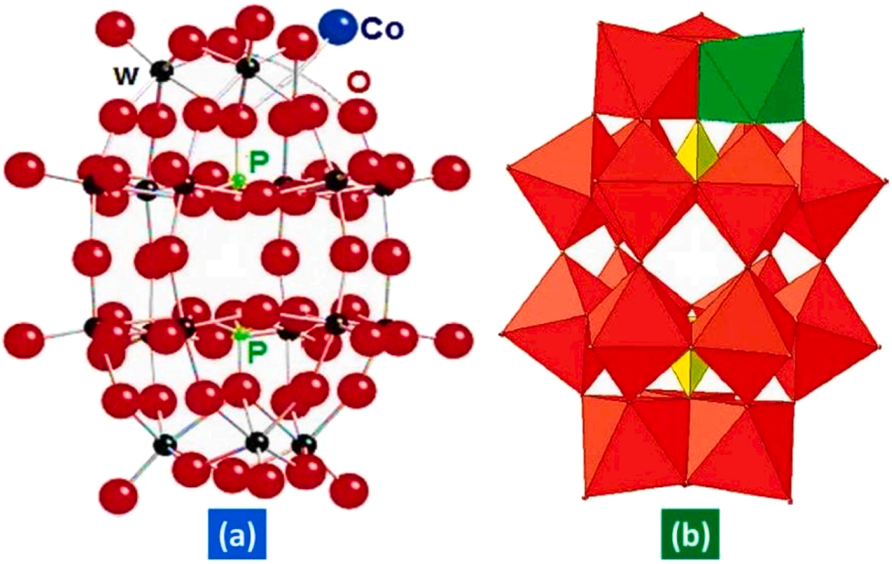

Fig. 1. (a) Balls and stick structure of the Wells-Dawson clusters polyoxometalate α_2-[$P_2W_{17}O_{61}$Co].Black represents tungsten; red represents oxygen; green represents phosphorus and blue represents substituted cobalt. (b) Polyhedral representation of POM structures tested in this study.

(b) homogeneous and/or heterogeneous-phase photocatalytic processes [24,25]; (c) sonochemical oxidation processes [26]; and (d) electrochemical oxidation processes [27].

Innovative methods include chemical oxidation using homogeneous-phase metal-based catalysts [28,29], which work by stimulating the oxidizing effect of H_2O_2 using these materials.

Hence, the advancement of selective oxidation systems employing H_2O_2 and durable inorganic catalysts featuring precisely organized polynuclear active sites can foster the progress of eco-friendly or ecologically conscious chemical processes.

Over the years, a multitude of catalytic oxidations using POMs and H_2O_2 have been produced. The POMs used for H_2O_2-based oxidations can be categorized into three groups based on their structures and the method of H_2O_2 activation: (a) di- and tetranuclear small peroxotungstates, (b) lacunary polyoxotungstates, and (c) transition-metal-substituted POMs [30].

Several catalytic oxidations using transition-metal-substituted polyoxometalates (POMs) have been created, and certain transition-metal-substituted POMs with precisely regulated active sites have demonstrated effective activation of H_2O_2 [31,32]. Polyoxometalates of the Wells-Dawson structural class, including their transition-metal-substituted derivatives, form a large and growing class of polyoxometalates (POMs). Their catalytic properties, such as thermal and hydrolytic stability, redox potential, charge density, acid-base properties, size and shape make these multifunctional POM-based materials particularly suitable for managing environmental problems [33–35]. These fundamental properties can be systematically modified and significantly tuned by modifying the constituent elements (charge-compensating cations, central atoms and framework polyatoms) [36]. These transition-metal-substituted POMs have attracted much attention as oxidation catalysts in several oxidation reactions [37–41].

Contant and co-workers were able to control metal substitution by (Mo^{VI}) and (V^{V}) by stereospecific preparation of lacunar species such as α_1-$[P_2W_{17}O_{61}]^{10-}$ and α_2-$[P_2W_{17}O_{61}]^{10-}$ from the Wells-Dawson complex α-$[P_2W_{18}O_{62}]^{6-}$ [42–44].

The purpose of this study was to investigate new characterizations, and the catalytic properties of a polyoxometalate complex formed by the introduction of (Co^{II}) ions into the monolacunary α_2-$[P_2W_{17}O_{61}]^{10-}$, which was already used as a catalyst in our previous study intended the degradation of dyes by $KMnO_4$ as an oxidizing agent [45].

The aim of this work was to study the efficiency of H_2O_2 to separately degrade indigo carmine and methyl orange in aqueous solution in the presence of $(\alpha_2P_2W_{17}O_{61}Co)^{8-}$ as catalyst. These toxic dyes are frequently used in industry, mainly in the textile and food industries [46–49], where their presence in industrial waste causes a noticeable change in the color and odor of water, even at very low concentrations.

However, to date, no reports have been published concerning the oxidation of indigo carmine and methyl orange by H_2O_2 using α_2-$[P_2W_{17}O_{61}Co]^{8-}$ as a homogeneous catalyst. The influence of different reaction parameters controlling the separate degradation of these dyes was investigated. The activity and stability of the α_2-$[P_2W_{17}O_{61}Co]^{8-}$ catalyst after several oxidation reaction cycles were also verified.

2. Materials and methods

2.1. Synthesis of polyoxometalates compounds

The lacunary compound $\alpha_2P_2W_{17}$, also known as $(\alpha_2K_{10}P_2W_{17}O_{61}.18H_20)^{10-}$, was synthesized from the saturated compound αP_2W_{18}, also known as $(\alpha K_6P_2W_{18}O_{62}.\cdot 20H_2O)^{6-}$, using the established methods described in the publications by Contant and Ciabrini [50] and Massart et al [51]. The chemical $\alpha_2P_2W_{17}$ was synthesized by removing the WO_4^{2-} group from αP_2W_{18}.

The catalyst $(\alpha_2K_8P_2W_{17}CoO_{61}.\cdot 19H_2O)$, also known as $\alpha_2P_2W_{17}Co$ (Fig. 1), was synthesized using the methodology described by Bartis et al [52]. A 10 ml (0.1 M) solution of $Co(NO_3)_3.\cdot 9H_2O$ was dissolved in 30 ml of water. Then, 4.7 g of $\alpha_2P_2W_{17}$ was added to the solution while stirring. The resulting product was precipitated by adding 20 ml of a saturated solution of KCl. Ultimately, the crystals that emerged were separated using filtration and subsequently dehydrated in ambient air.

2.2. Characterization of polyoxometalates compounds

The UV–vis spectroscopy measurements were conducted using a JENWAY 6705 digital spectrophotometer. Quartz containers with a 10 mm distance for light to pass through were utilized.

The infrared spectroscopy data were recorded using an FT-IR spectrometer model K800A-MY14400002. The spectra were analyzed using the Agilent resolution Pro program.

The X-ray diffraction patterns were obtained by utilizing a RIGAKU model D/max 2500 diffractometer, which was configured in the Bragg-Brentano setup and equipped with an anticathode Cu (1.541874 A°) X-

Table 1
Chemical structures and characteristics of IC and MO dyes.

Dye	Structure	Mw ($g.mol^{-1}$)
Indigo Carmine	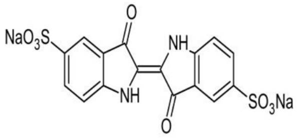	466.353
Acid Orange	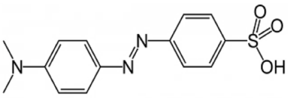	327.33

ray tube. The acquisition circumstances relate to a range of angles, specifically from 5 to 90 °degrees.

The surface morphologies were analyzed using a QUANTA 250 Microscope, fitted with an Energy Dispersive X-ray (EDX) spectroscopy instrument, through the technique of Field Emission Scanning Electron Microscopy (FE-SEM).

2.3. Oxidation of dyes

2.3.1. Chemical reagents

Indigo carmine (IC), also known as cotton blue or acid blue 93, with a molecular formula of $C_{37}H_{27}N3Na_2O_9S_3$, and Methyl orange (MO), also known as Acid Orange 52, helianthine B, Orange III, Gold orange, and Tropaeolin D, with a molecular formula of $C_{14}H_{14}N_3NaO_3S$, were employed as model compounds. The IC and MO compounds were provided by Sigma-Aldrich without undergoing any purification process. The chemical structures and properties are presented in (Table 1). The hydrogen peroxide (H_2O_2) utilized in this investigation was acquired from Merck Chemical Company. The remaining reagents (NaOH and H_2SO_4) utilized in this investigation were of analytical quality.

2.3.2. Procedure for the oxidation of the IC and MO dyes

The oxidation of IC and MO was carried out individually in batch reactor of 200 mL at ambient temperature. An adequate quantity of catalyst ($\alpha_2P_2W_{17}Co$) was added to 100 mL of dye solutions (MO) or (IC) with initial concentrations of 10 mg/L. In all trials, the beginning concentrations of dyes were maintained at a constant level, except for those conducted specifically to investigate the impact of varying initial dye concentrations. The pH of the reaction was modified using (0.1 M) H_2SO_4 or (0.1 M) NaOH in aqueous solutions with the aid of a HANNA pH meter. An electromagnetic stirrer was employed to guarantee homogeneous blending of the aqueous solution. Subsequently, a specific amount of the oxidant (H_2O_2) with a defined concentration was introduced. Currently, the oxidation reaction was started. During the initial stages of the reaction involving IC or MO, a 2 mL sample was obtained from the reactor every 2 min. The absorbance of dyes in the sample was measured using a JENWAY 6705 UV–vis spectrophotometer. The wavelength at which (IC) exhibits the highest absorbance is 611 nm, as reported by Grabsi et al [45]. It is worth noting that this dye demonstrates exceptional stability in an aqueous environment. However, the color of the MO changes depending on the pH of the medium. To estimate the maximum wavelength (λ_{max}) of the MO, the absorbance of the MO solution was measured at different pH levels within the range of 400–800 nm [37]. The oxidation of dyes was conducted based on the following parameters: initial pH of the solution, concentration of the oxidant, concentration of the catalyst, and initial concentration of the dye. The impact of temperature, presence of inorganic salts, and kind of particulate organic matter (POMs) was also investigated. The percentage of dye degradation efficiency was estimated as follows:

$$DE(\%) = \frac{C_i - C_f}{C_i} \times 100 \tag{1}$$

Where: DE (%) is the degradation efficiency; C_i (mg/L) is the initial concentration of dyes and C_f (mg/L) is the final concentration of dyes.

After calculation, we found a limit of detection (LOD) of 0.81 for indigo carmine and 1.02 for methyl orange.

The percentage error obtained is 2.63 % for indigo carmine and 1.66 % for methyl orange. These results indicate that the measured values are very close to the values predicted by the linear regression model, confirming the good accuracy of the measurements in relation to the model.

3. Results and discussion

3.1. Characterization of polyoxometalates compounds

3.1.1. Phase structure of POMs nanoparticles

X-ray powder diffraction at room temperature is commonly used to examine the structural characteristics of POMs and to explain their properties [53]. This study aims to identify the crystalline phases present in the three samples analyzed. All the structural parameters deduced from the X-ray diffraction (XRD) data are summarized in (Table 2). (Fig. 2) shows the X-ray diffractograms of the three Dawson-based POMs. Peaks were analyzed and indexed by the Search-Match method using Crystal Impact Match software and the Crystallography Open Database (COD-Inorganics 2020.12.16).

According to the results, parent and lacunar POMs could indeed lead to the formation of the P/W/O phases (entry number: 96–231–0828) [61], and P/W/O/H phases (entry number: 96–210–6441) [59], where rearrangement could occur due to significant structural transformation. Removal of the WO_4^{2-} group leads to significant fragmentation of the structure, resulting in partial amorphization of the P_2W_{17} gap structure. This creates a point defect in the structure, rendering P_2W_{17} partially amorphous with a mixed (amorphous and crystalline) structure, as evidenced by the enlarged bumps and overlapping peaks observed.

The monosubstituted Co-POM exhibits a structural rearrangement, as shown by the predominant formation of a Dawson phase (entry number: 96–231–0828) [61], and the presence of traces of Keggin phases. We also observe the formation of a new phase (Co/O) (entry number:96–152–6827 and 96–152–6823) [62], logically resulting from the addition of cobalt. These new cobalt phases crystallize in the orthorhombic and monoclinic systems with space groups (Ccmm) and (C12/m1) respectively. The formation of these new phases results from the reorganization of tungsten and phosphorus oxides due to the creation of vacancies, and is potentially influenced by the presence of alkali metal Co(II). The addition of Co(II) appears to improve the degree of crystallinity. The resulting compound exhibits distinct acid and redox sites due to its unique structural properties, which may affect catalytic performance.

It is entirely possible for a Dawson-type POM to contain a Keggin-type fragment or subunit. This coexistence of phases results from partial structural transformations, creating mixed structures with new and interesting properties [54]. These transformations can also occur because Keggin units are often more stable or thermodynamically favored under certain conditions.

Additional UV–Vis and FT-IR characterizations were carried out in the previous study [45], showing that the Dawson phase is in the majority in the sample. This is also confirmed by the atomic ratios W/P/O/Co in the chemical composition determined by EDX and elemental analysis presented in this study. This is also evident in the Co-POM diffractogram, which is identical to those of Dawson-structured Cu-POM and Ni-POM presented in the related literature [55,56].

3.1.2. Determination of crystallite size

X-ray diffraction can be used not only to identify the crystalline

Table 2
Crystal data and structural parameters of POMs phases.

α- [$P_2W_{18}O_{62}$] .20H_2O

Name phase	**$O_{62}P_2W_{18}$**	**$O_{47}W_{17}$**	**$O_{14}W_5$**	**$H_{45}O_{61}PW_{12}$**	**$O_{2.72}W$**	**$O_{49}W_{18}$**
Entry number	96-231-0828	96-210-7066	96-152-7784	96-210-6441	96-153-8316	96-100-1679
FoM	0.780552	0.660434	0.612845	0.645521	0.618036	0.618036
Intensity scale factor	0.67	0.20	0.08	0.09	0.04	0.04
Space group	P -1	P 1 2/m 1	P -4 21 m	P c c a	P 1 2/m 1	P 1 2/m 1
Crystal system	triclinic	Monoclinic	Tetragonal	Orthorhombic	Monoclinic	Monoclinic
a (Å)	12.8600	18.8400	23.3300	20.7880	18.3200	18.3200
b (Å)	14.8300	3.7870	-	13.0860	3.7900	3.7900
c (Å)	22.3400	12.3300	3.7970	18.8790	14.0400	14.0400
α (deg)	94.400	-	-	-	-	-
β (deg)	116.870	102.670	-	-	115.030	115.030
ϒ (deg)	115.600	-	-	-	-	-
cell volume(Å^3)	3225.59	858.29	2066.67	5135.69	883.28	879.46
Z	2	1	8	4	18	1
I/Ic	4.43	7.60	7.05	15.22	7.80	7.80
Calc. Density (g/cm^3)	4.492	7.501	7.348	4.214	7.695	7.695
Amount (%)	74.5	12.6	5.3	2.7	2.6	2.3
Reference	[51]	[54]	[55]	[56]	[57]	[58]
Total cristalinity (%)			80.36			

α_2- [$P_2W_{17}O_{61}$] .18H_2O

Name phase	**$O_{62}P_2W_{18}$**	**$H_{45}O_{61}PW_{12}$**
Entry number	96-231-0828	96-210-6441
FoM	0.780552	0.645521
Intensity scale factor	0.67	0.09
Space group	P -1	P c c a
Crystal system	triclinic	Orthorhombic
a (Å)	12.8600	20.7880
b (Å)	14.8300	13.0860
c (Å)	22.3400	18.8790
α (deg)	94.400	-
β (deg)	116.870	-
ϒ (deg)	115.600	-
cell volume(Å^3)	3225.59	5135.69
Z	2	4
I/Ic	4.43	15.22
Calc. Density (g/cm^3)	4.492	4.214
Amount (%)	59.5	40.5
Reference	[51]	[56]
Total cristalinity (%)		62.58

α_2- [$P_2W_{17}O_{61}Co$] .19H_2O

Name phase	**$O_{69}PW_{12}$**	**$H_{45}O_{61}PW_{12}$**	**$O_{73}W_{25}$**	**$Co_{0.885}$ O_2**	**CoO_2**	**$O_{62}P_2W_{18}$**
Entry number	96-901-5518	96-210-6441	96-210-6890	96-152-6827	96-152-6823	96-231-0828
FoM	0.668780	0.645521	0.607392	0.624153	0.621464	0.780552
Intensity scale factor	0.38	0.09	0.28	0.35	0.35	0.67
Space group	F d -3 m	P c c a	P 1 2/c 1	C 1 2/m 1	C c m m	P -1
Crystal system	Cubic	Orthorhombic	Monoclinic	Monoclinic	Orthorhombic	Triclinic
a (Å)	23.2800	20.7880	11.9300	4.8360	4.8340	12.8600
b (Å)	-	13.0860	3.8200	2.8200	2.8200	14.8300
c (Å)	-	18.8790	59.7200	32.4730	21.5180	22.3400
α (deg)	-	-	-	-	-	94.400
β (deg)	-	-	98.300	95.840	-	116.870
ϒ(deg)	-	-	-	-	-	115.600
cell volume(Å^3)	12612.79	5135.69	2693.09	440.55	293.33	3225.59
Z	4	4	2	6	4	2
I/Ic	35.95	15.22	7.02	30.06	32.55	4.43
Calc. Density (g/cm^3)	3.518	4.214	7.108	1.903	2.059	4.492
Amount (%)	3.4	10.9	13.2	3.8	3.5	59.5
Reference	[59]	[56]	[60]	[52]	[52]	[51]
Total cristalinity (%)			96.02			

structure, but also to assess the average size of crystallites. Extracting size and strain independently from the full width at half maximum (FWHM) of X-ray diffraction (XRD) peaks is not highly reliable. Therefore, we choose to use the well-established Modified Scherrer Method and Hall-Williamson methods instead.

Scherrer Method: Scherrer has formulated an Eq. (2) to quantify the widening of x-ray diffraction peaks solely caused by the presence of small crystallite sizes.

$$D = \frac{K\lambda}{\beta \cos\theta} \qquad (2)$$

Where λ is the wavelength of the x-rays used, θ is the Bragg angle, D is the "average" crystallite size measured in a direction perpendicular to the surface of the specimen, and kis a constant. This equation is commonly known as the Scherrer equation [63].

Modified Scherrer Method: The modified Scherrer formula utilizes

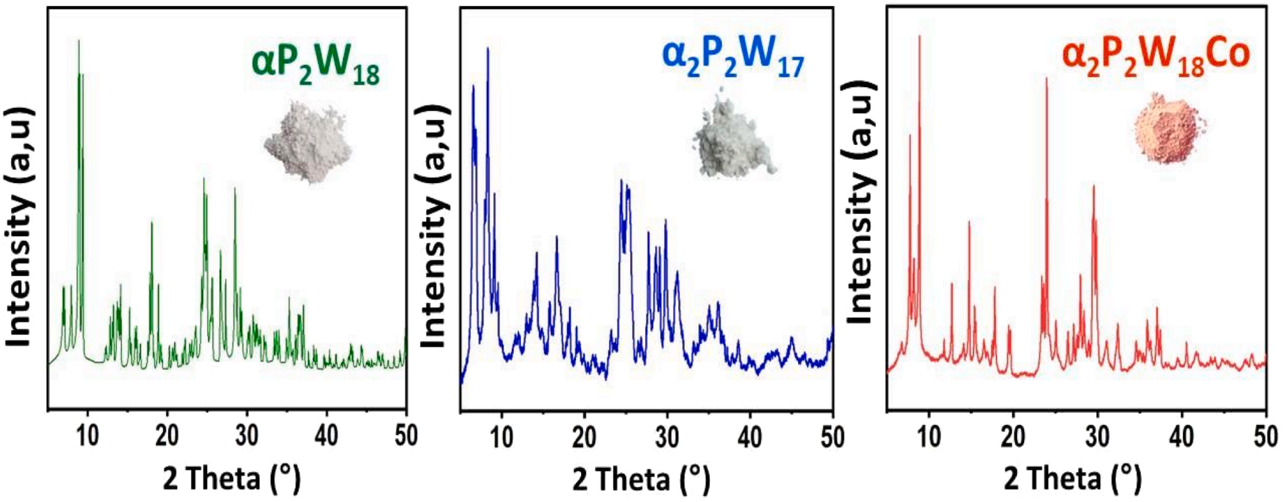

Fig. 2. Powder X-ray diffraction patterns of the POMs nanocomposites.

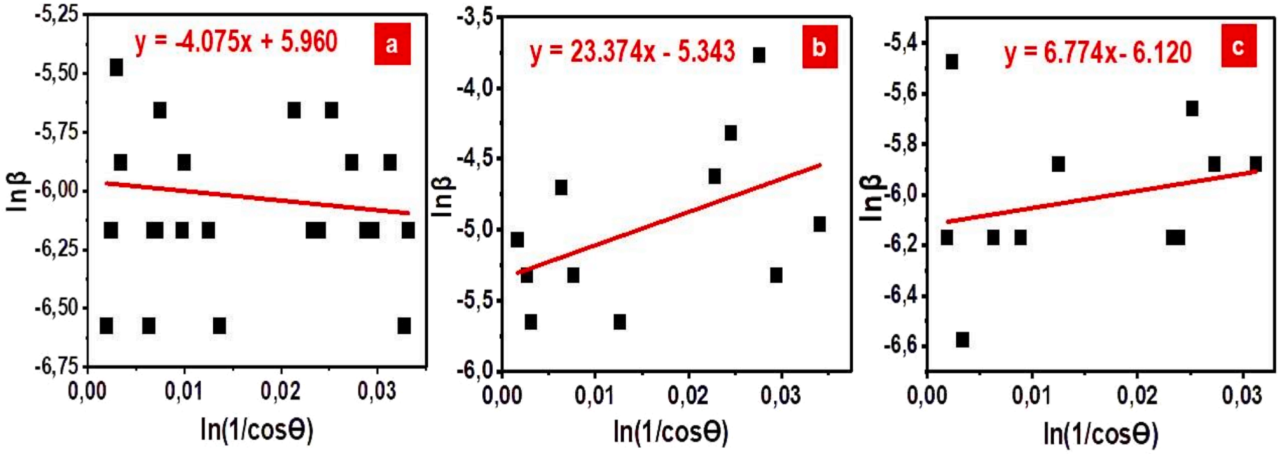

Fig. 3. Modified Scherrer plot of POMs nanocomposites. Crystallite size D is extracted from y-intercept. (a) parent POM; (b) lacunary POM; (c) Co-POM.

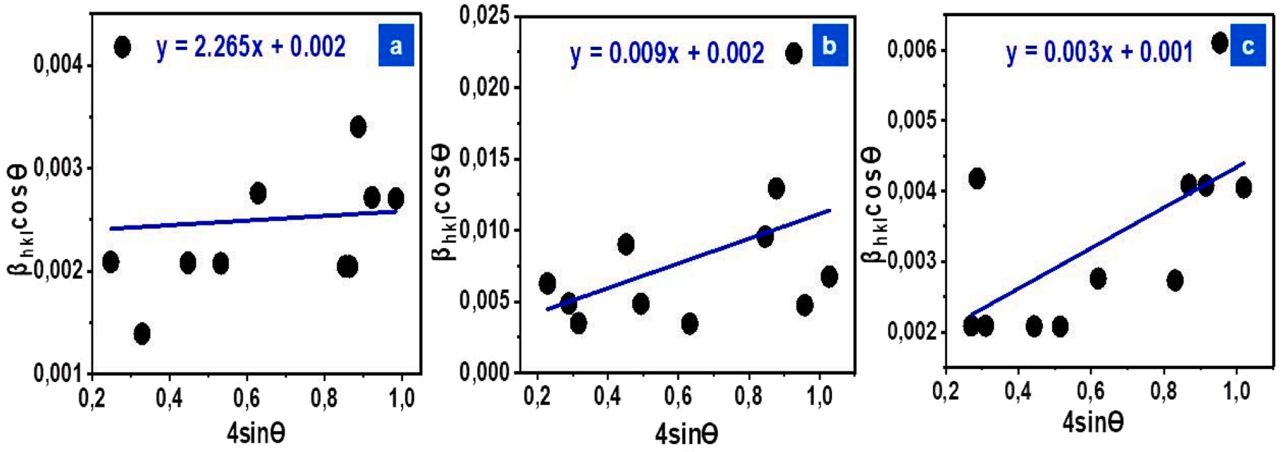

Fig. 4. Williamson–Hall plots (UDM method) for POMs nanocomposites. The strain is extracted from the slope and the crystallite size D is extracted from y-intercept. (a) parent POM; (b) lacunary POM; (c) Co-POM.

the least square method to reduce error in computing the crystallite size and finding the average value of D from all main peaks [63]. The Scherrer formula can be expressed as follows:

$$\ln\beta(\mathrm{D}) = \ln\left(\frac{\mathrm{K}\lambda}{\mathrm{D}}\right) + \left(\frac{1}{\cos\theta}\right) \tag{3}$$

Now by plotting a graph between $ln\beta_{hkl}(\mathrm{D})$ and $ln(1/\cos\theta)$, a straight

Table 3
X-ray diffraction data and cristallite size of POMs compounds.

POM	2 Θ (deg)	d (Å)	Peak height	Peak area	FWHM (β)		Scherrer's (D) (nm)	Average (D) (nm)	Hall- Williamson (D) (nm)	Modifed Scherrer's (D) (nm)
					deg	Rad				
aP_2W_{18}	7.1	12.4	196.1	531.60	0.12	0.0021	66.35	48.34	57.77	56.12
	8.0	11.1	268.2	1454.1	0.24	0.0042	33.19			
	9.3	9.4	853.1	1542.0	0.08	0.0014	66.40			
	12.8	6.9	155.9	422.50	0.12	0.0021	66.61			
	15.0	5.8	177.3	480.60	0.12	0.0021	66.76			
	18.1	4.9	455.9	1647.9	0.16	0.0028	50.26			
	24.7	3.6	492.4	1335.0	0.12	0.0021	40.58			
	24.9	3.6	516.9	1401.4	0.12	0.0021	50.76			
	25.5	3.5	215.7	974.60	0.20	0.0035	33.91			
	26.6	3.3	333.7	1206.5	0.16	0.0028	22.72			
	28.8	3.1	558.4	2018.8	0.16	0.0028	34.23			
$\alpha_2P_2W_{17}$	6.5	13.5	946.6	4308.5	0.36	0,0063	22.10	23.25	45.46	30.30
	8.2	10.7	1000	3540.1	0.28	0,0049	28.45			
	9.1	9.7	457.6	1157.5	0.20	0,0035	39.85			
	13.7	6.8	164.8	1083.5	0.52	0,0091	15.38			
	14.2	6.2	343.6	1216.5	0.28	0,0049	28.59			
	18.2	4.9	149.7	378.60	0.20	0,0035	40.23			
	24.3	3.6	623.5	4414.6	0.56	0,0098	14.51			
	24.5	3.5	597.7	5742.8	0.76	0,0133	10.71			
	25.2	3.3	141.0	2353.5	1.32	0,0230	6.19			
	27.6	3.2	433.9	1536.0	0.28	0,0049	29.22			
	29.8	3.0	469.2	2372.9	0.40	0,0070	20.55			
$\alpha_2P_2W_{17}Co$	7.6	11.4	670.34	2267.2	0.12	0,0021	49.65	59.28	92.28	65.88
	8.1	10.8	357.70	2419.6	0.24	0,0042	66.20			
	8.9	10.0	1000	3382.1	0.12	0,0021	33.10			
	12.7	7.0	263.59	891.50	0.12	0,0021	99.30			
	14.7	6.0	439.17	1485.3	0.12	0,0021	66.20			
	17.9	5.0	263.19	1186.8	0.16	0,0028	66.20			
	24.0	3.8	262.37	1478.9	0.20	0,0035	49.65			
	24.9	3.7	913.75	4120.5	0.16	0,0028	66.20			
	25.1	3.6	170.51	1153.4	0.24	0,0042	66.20			
	27.5	3.2	126.95	1288.1	0.36	0,0063	39.72			
	29.3	3.0	516.78	3495.6	0.24	0,0042	49.65			

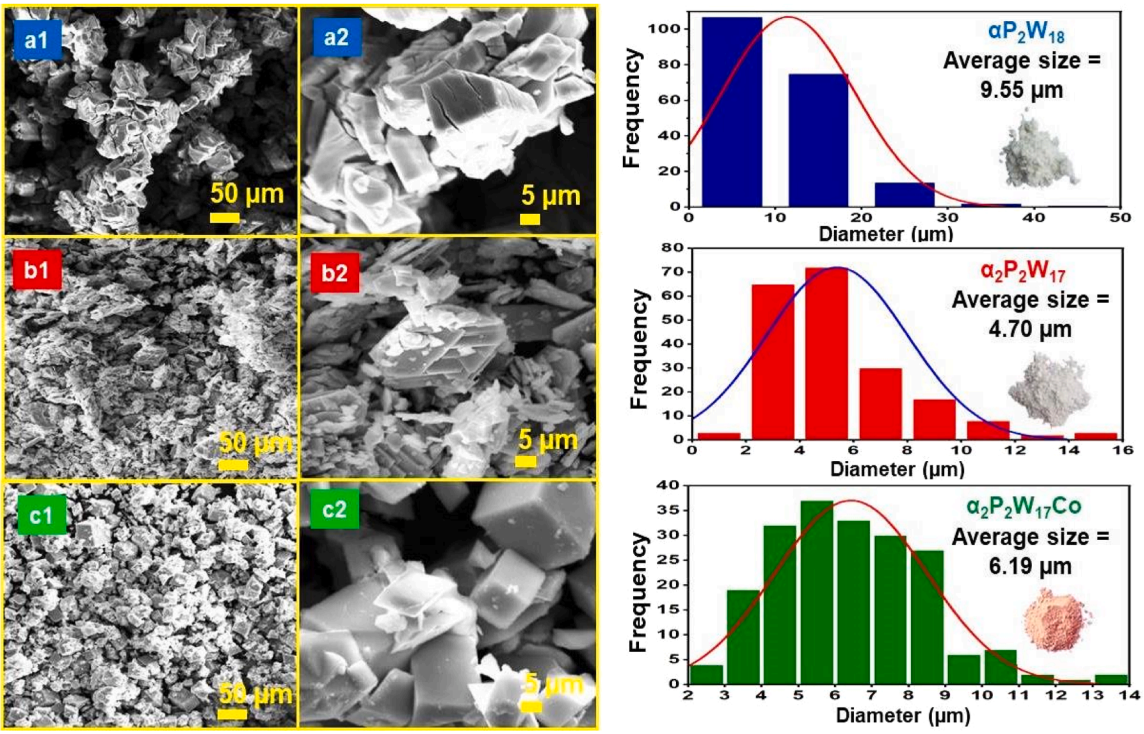

Fig. 5. FE-SEM micrographs and illustration show particle size histogram of nanocomposites. (a) parent POM; (b) lacunary POM; (c) Co-POM.

Table 4
Elemental composition of sample (identified crystalline phases only).

Element Amount (%)	P_2W_{18}	P_2W_{17}	$P_2W_{17}Co$
P	0.59	0.56	0.06
H	2.65	1.23	0.02
O	37.43	25.65	88.13
W	59.88	72.55	8.69
Co	–	–	3.09
Total (%)	100	100	100

line with an intercept equal to ln(kλ/D) is obtained (Fig. 3).

Williamson-Hall plot method: The equations (4) above represent the W-H equations, which utilize the uniform deformation model (UDM).

$$\beta=\beta(\mathrm{D})+\beta(\varepsilon) \text{ or } \left(\frac{\beta\cos\theta}{\mathrm{K}\lambda}\right)=\left(\frac{1}{\mathrm{D}}\right)+\left(\frac{4\varepsilon\sin\theta}{\mathrm{K}\lambda}\right) \tag{4}$$

The plot βcosθ/kλ versus 4sinθ/kλ should be a straingt line, where the slope provides the strain in the sample and the y axis provides the inverse of average crystallite size in the materials.

The plot is represented by the equation 4sinθ/kλ versus βcosθ/kλ. The strain and average crystallite size are determined by analyzing the slope and intercept, respectively [64]. The UDM analysis for three POMs is displayed in (Fig. 4).

The results obtained with the three methods corroborate each other and show a clear deformation of the structure. This supports the SEM analysis presented in the previous study [45], which indicates a variation in grain size. The crystallite size of the monolacunar phase is smaller than that of the parent POM and Co-POM; the latter showing a larger average crystallite size using all three methods. However, the average crystallite size obtained from the Scherrer formula, the Modified Scherrer Method and the W-H analysis (Table 3) shows a greater variation because of the difference in averaging the particle size distribution [65].

3.1.3. Size distribution and morphology of POMs nanoparticles

The morphological and particle size distributions were determined based on the digital pictures acquired. The average diameter of the POMs was estimated using a set of 200 grains selected from arbitrary areas of the magnified micrographs. The grain sizes in the micrographs were quantified using Image J software (version 1.53e). The average grain sizes of the three samples are depicted by the histogram in (Fig. 5).

From the SEM images shown in (Fig. 5), we can also observe a deformation of the microstructure, manifested by a change in the grain geometry of each POM. This observation is in line with the XRD analysis presented earlier, which shows a clear variation in the crystallite size of the three POMs.

Co-POM grains appear to be more homogeneous than those of the other two POMs, most being between 3 and 4 µm in size. Co-POM grains show a uniform distribution with almost identical sizes, being evenly dispersed and well-crystallized, with a cubic or pseudo-cubic morphology. This morphology confers a high specific surface area, which logically translates into enhanced catalytic activity.

Significantly, the micrographs (Fig. 5) show a morphological change during synthesis, where the majority of P_2W_{18} and P_2W_{17} grains are characterized by an aggregate of irregular polyhedral shapes, which cluster to form agglomerates. It is clear that the incorporation of Co(II) ions into the lacunar POM considerably reduced the grain size (from 9.55 to 6.19 µm) at the end of synthesis.

3.1.4. Elemental composition analysis

In this study, we used a different analytical technique to that used in our previous study to analyze the chemical composition of the three materials. This technique is based on the quantification of chemical elements that are present only in the crystalline phases of the structure of each POM. The (Table 4) confirms the result obtained by EDX elemental analysis in the previous study [45], where the presence of high proportions of the elements P, O, and W in the total crystalline structure of the three POMs was consistently confirmed. In the case of the mono-substituted Co-POM, the contribution of the added metal element (Co^{II}) to the crystallization of the complex is well verified. The appearance of hydrogen (H) in this analysis is due to the crystallization of the water molecule (H_2O) in the structure of the samples studied.

3.2. Oxidation of dyes

3.2.1. Effects of the operating parameters on IC and MO degradation

The catalytic activity of a catalyst is generally influenced by various reaction parameters. In order to obtain the optimum degradation yield for indigo carmine and methyl orange, an in-depth study to optimize the experimental conditions for oxidation was undertaken. Several parameters were examined.

3.2.1.1. Effect of pH. The pH of the medium is a crucial factor in advanced oxidation processes, as it significantly influences degradation efficiency, as well as the stability and activity of catalysts in aqueous solution [24–27]. The results are illustrated in (Fig. 6):

The results presented in (Fig. 6) show that maximum degradation of both dyes was observed at acidic pH (pH = 3), with a maximum

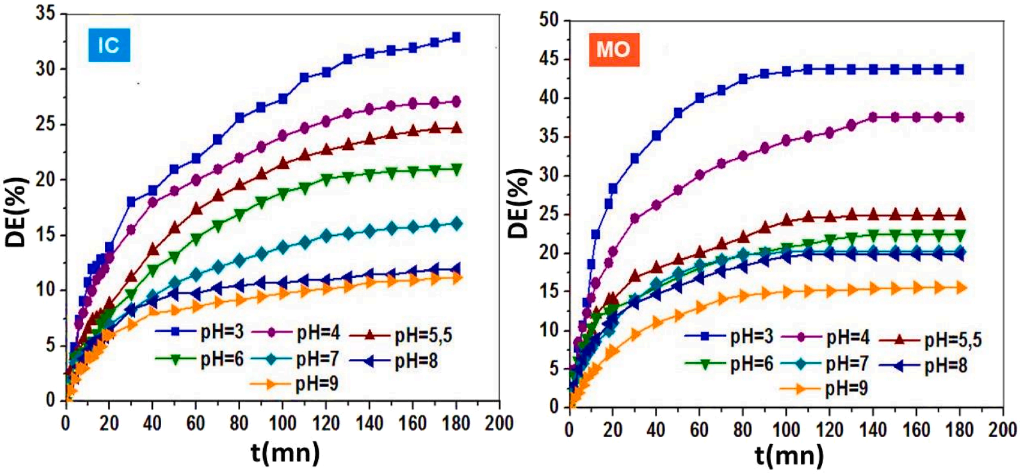

Fig. 6. Effect of pH on the degradation process using the (H_2O_2/Co-POM) system ($[Dye]_0$ = 10 mg/L, [cat]=0.2mM, $[H_2O_2]$ = 0,077 M, T=25 °C).

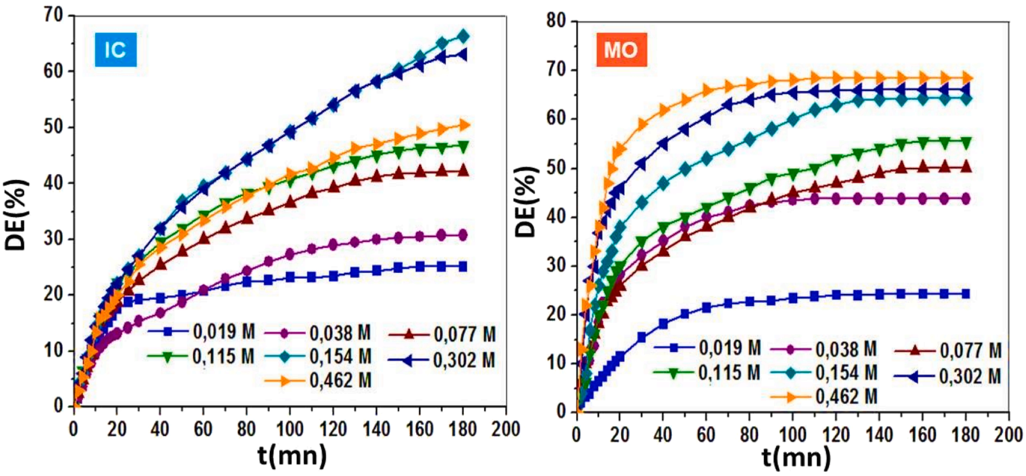

Fig. 7. Effect of H_2O_2 concentration on the degradation process using the (H_2O_2/Co-POM) system (pH=3, $[Dye]_0$=10 mg/L, [cat]=0.2mM, T=25 °C).

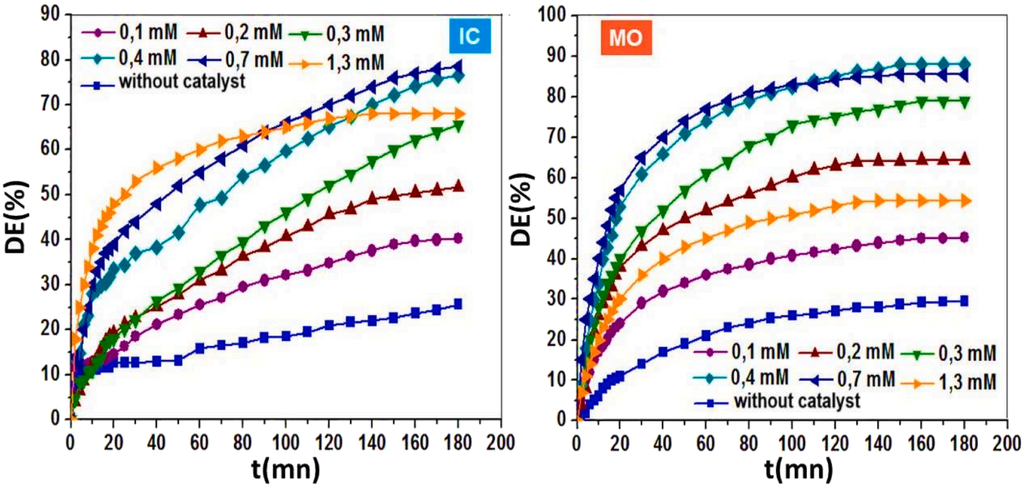

Fig. 8. Effect of catalyst concentration on the degradation using the (H_2O_2/Co-POM) system (pH=3, $[H_2O_2]$ =0.154 M, $[Dye]_0$ =10 mg/L, T=25 °C).

degradation efficiency of 32.93 % for IC and 43.74 % for MO. Degradation efficiency increased with decreasing pH.

These results are corroborated by several studies [37,39,40], which indicate that this value (pH = 3) corresponds to the optimum rate of H_2O_2 decomposition into hydroxyl radicals $OH^{\bullet}$. Moreover, in aqueous solution, the majority of Dawson-type POMs are stable only in acidic media [66]. It is also important to note that POMs possess Brønsted acidity, and that H^+ protons act as catalytically active sites. Consequently, a shift to a neutral or basic medium may result in a loss of their acidic properties, due to a decrease in the accessibility of H^+ protons and thus a reduction in the strength of the active acid sites [67].

The decrease in efficiency under basic conditions may be due to a deactivation of the catalytic effect of the substituted transition metal (Co^{II}), caused by the precipitation of cobalt ions in the form of cobalt hydroxide $Co(OH)_2$ according to the following reaction:

$$Co^{2+}_{(aq)} + 2OH^-_{(aq)} \rightarrow Co(OH)_{2(s)} \quad (5)$$

Furthermore, in strongly alkaline media, hydrogen peroxide (H_2O_2) is susceptible to decomposition into H_2O and O_2 [68], resulting in a decrease in the production of $OH^{\bullet}$ radicals required for optimal degradation of organic matter.

3.2.1.2. Effect of H_2O_2 concentration. According to the literature [69], activation of H_2O_2 by homogeneous catalysts is attributed to the formation of OH^- hydroxyl radicals, which are highly reactive. This activation occurs via decomposition of H_2O_2, resulting in homolytic cleavage of the molecule's O-O bond, leading to the formation of these $OH^{\bullet}$, which can react with organic molecules [70]. (Fig. 7) illustrates the degradation efficiency of indigo carmine (IC) and methyl orange (MO) at different concentrations of H_2O_2.

Degradation efficiency increased with H_2O_2 concentration up to a critical concentration of 0.154 M for indigo carmine and 0.302 M for methyl orange, where degradation efficiency reached its maximum, namely 66.34 % and 66.18 % for the two dyes respectively. Above this critical concentration, degradation efficiency decreased (Fig. 7). This phenomenon, commonly observed in H_2O_2-based oxidation processes, is known as the $OH^{\bullet}$ radical trapping effect [71]. This decrease is mainly due to the excess of H_2O_2, which promotes competing undesirable reactions to the oxidation of pollutants, through the recombination of $OH^{\bullet}$ radicals on the one hand (Eq 6), and through the reaction between $OH^{\bullet}$ radicals and H_2O_2 on the other (Eq 7), producing an inhibitory effect according to the following reactions [72]:

$$OH^{\bullet} + OH^{\bullet} \rightarrow H_2O_2 \quad (6)$$

$$H_2O_2 + OH^{\bullet} \rightarrow H_2O + HO_2^{\bullet} \quad (7)$$

$$HO_2^{\bullet} + OH^{\bullet} \rightarrow H_2O + O_2^{\bullet} \quad (8)$$

A solution concentrated in H_2O_2 leads to the extinction of $OH^{\bullet}$

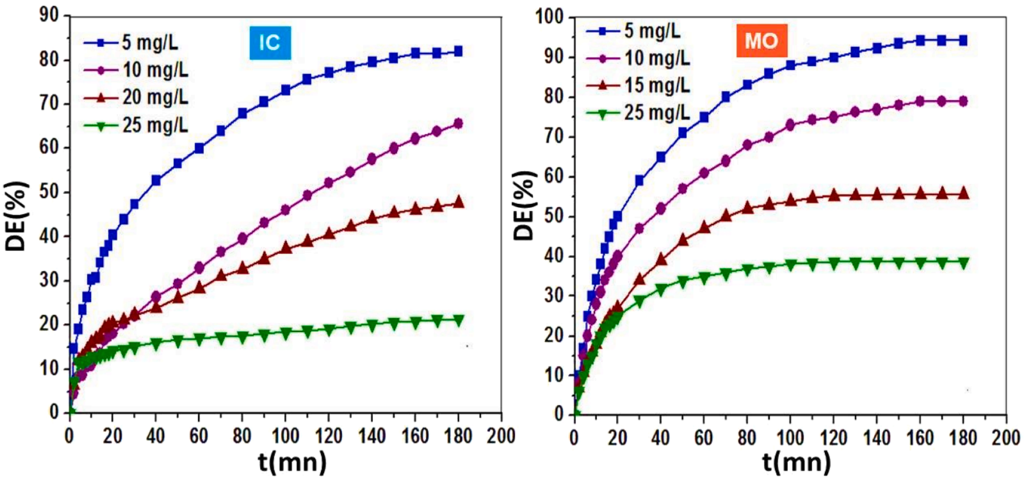

Fig. 9. Effect of dye concentration on the degradation using the (H_2O_2/Co-POM) system (pH=3, [H_2O_2]=0.154 M, [cat]=0.3mM, T=25 °C).

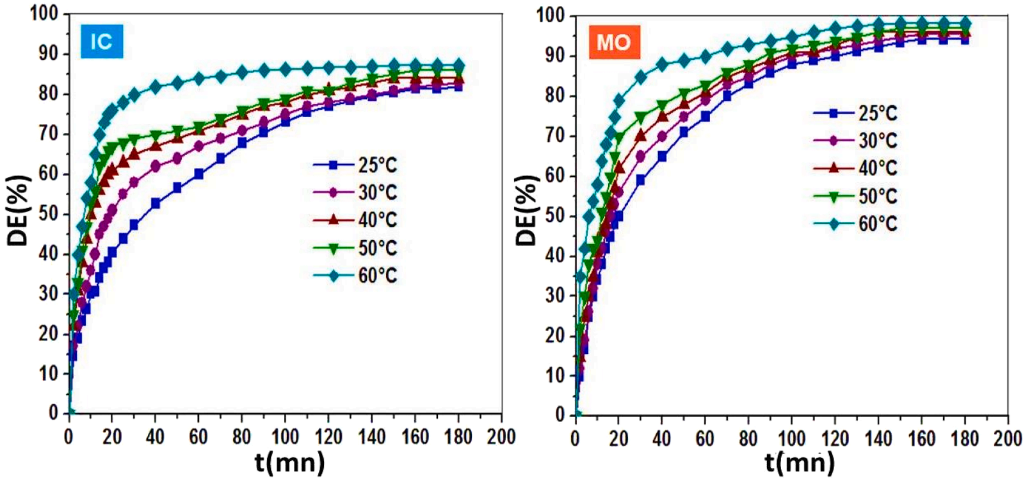

Fig. 10. Effect of temperature on the degradation using the (H_2O_2/Co-POM) system temperature (pH=3, [Dye]= 5 mg/L, [cat]= 0.3mM, [H_2O_2] = 0.154 M).

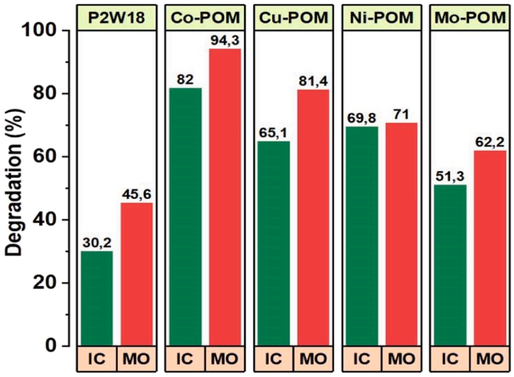

Fig. 11. Effect of the catalyst type on the degradation efficiency (pH=3, [Dye]= 5 mg/L, [cat]= 0.3mM, [H_2O_2] = 0.154 M, T=25 °C).

hydroxyl radicals by the formation of $HO_2^{\bullet}$ hydroperoxyl radicals and superoxydes ($O_2\bullet$) (Eq 8). However, these intermediate species are less reactive, as their oxidation potential is much lower than that of $OH^{\bullet}$ radicals [73].

At low oxidant concentrations, H_2O_2 does not produce sufficient $OH^{\bullet}$ radicals, which logically translates into reduced degradation efficiency. Moreover, the majority of free radicals produced are directly consumed by organic matter, making them insufficient for the complete oxidation of pollutant molecules present in the reaction medium. Several authors point out that, at high concentrations, H_2O_2 can become an $OH^{\bullet}$ radical extractor [74]. Consequently, the concentration of 0.154 M H_2O_2 was chosen as the optimum concentration and was considered thereafter.

3.2.1.3. *Effect of the catalyst concentration.*

The majority of published work in the field of homogeneous POM catalysis indicates that there is always an optimum catalyst concentration where the oxidation efficiency reaches its maximum [75]. Moreover, for economic reasons, it is important to avoid an excess of catalyst.

The study of the effect of the catalyst on the degradation of indigo carmine (IC) and methyl orange (MO) was carried out using the system ($P_2W_{17}Co$/H_2O_2/pollutant) by varying the concentrations of P_2W_2Co from 0.1 to 1.3 mM, while maintaining optimal experimental conditions (pH = 3, [H_2O_2] = 0.154 M).

(Fig. 8) shows that increasing the concentration of $P_2W_{18}Co$ promoted the degradation of both dyes in the range of 0.1 to 0.7 mM for IC and 0.1 to 0.4 mM for MO, where the maximum degradation efficiency reached 78.5 % and 88.02 % respectively. These results are in line with several studies [38,76], which explain that this improvement is due to an increase in the number of active sites in the catalyst, resulting in greater production of $OH^{\bullet}$ radicals, responsible for oxidation. However, above 0.7 mM for IC and 0.4 mM for MO, a decrease in efficiency was

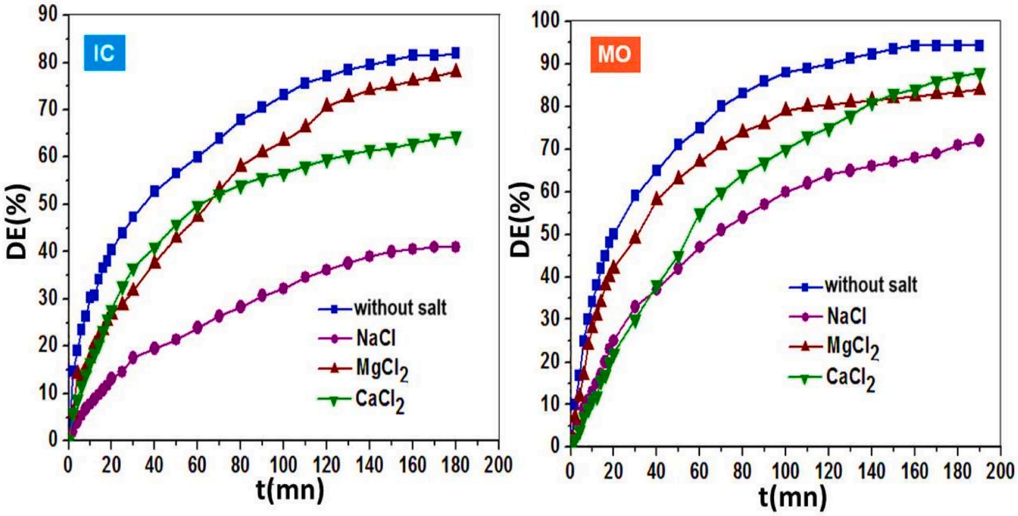

Fig. 12. Effect of chloride salts on degradation efficiency.

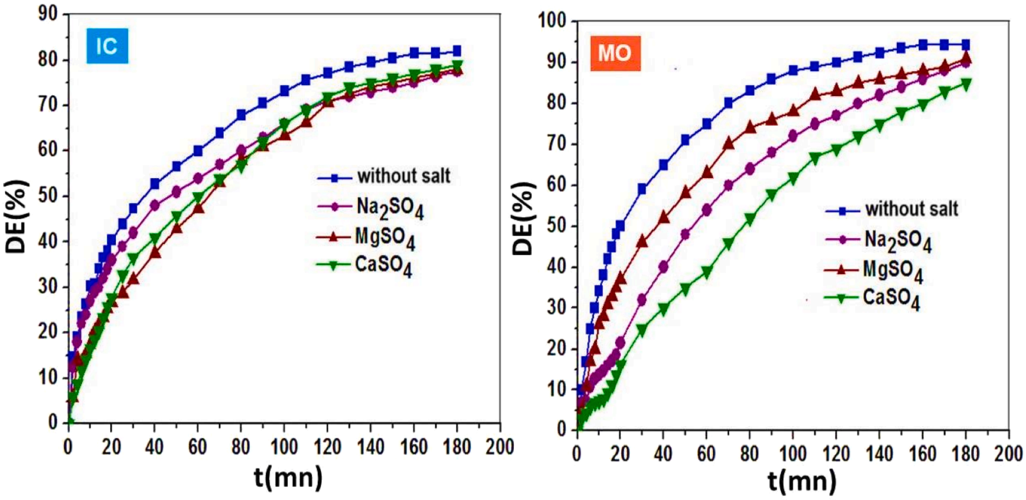

Fig. 13. Effect of sulfate salts on degradation efficiency.

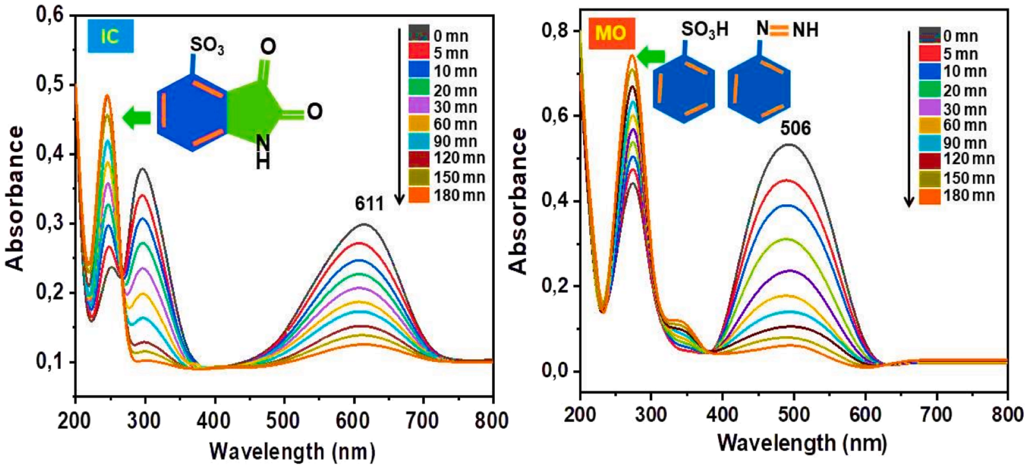

Fig. 14. Time-dependent UV–vis absorption spectra of indigo carmine and methyl orange degraded by homogeneous system (H_2O_2/Co-POM).

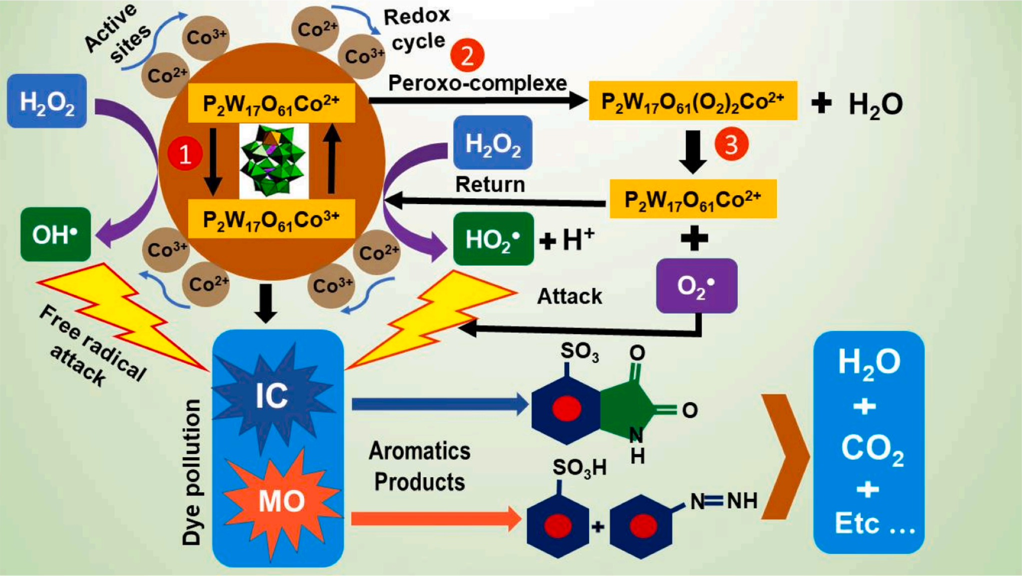

Fig. 15. Proposed mechanism of catalytic degradation of dyes using the homogeneous system (H_2O_2/Co-POM).

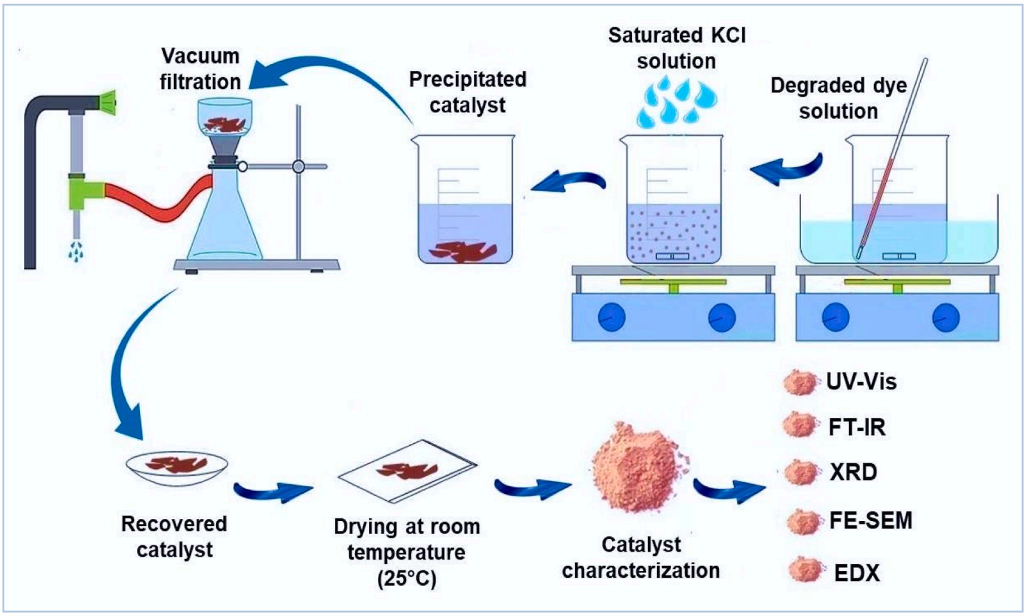

Fig. 16. Recovery steps and characterization of the catalyst after five operating test cycles.

observed, from 78.5 % to 68.12 % for IC and from 88.02 % to 54.41 % for MO.

Furthermore, it has been found that no further improvement in efficiency is achieved with an excessive increase in the amount of catalyst, due to parasitic reactions that consume hydroxyl radicals [77]. Furthermore, the presence of an excess of Co-POM particles relative to dye molecules increases the probability of dye molecule suspension, creating an inhibitory barrier that reduces degradation efficiency. In conclusion, an excess of catalyst does not improve the degradation process and may even be counterproductive.

3.2.1.4. Effect of dye concentration. (Fig. 9) shows that increasing the initial pollutant concentration, in the range 5–25 mg/L, led to a significant decrease in degradation efficiency, while an increase in residual dye concentration was observed. These results can reasonably be interpreted by an insufficient degradation for high-concentration color solutions.

Other authors have obtained similar results [78], attributed to the fact that, under high dye concentrations, the number of $OH^{\bullet}$ radicals produced in the dye solution becomes insufficient. In other words, the decrease in efficiency may be due to the rapid and increased consumption of $OH^{\bullet}$ hydroxyl radicals by the dye molecules concentrated in the solution. In addition, the amount of residual intermediates, which also consume $OH^{\bullet}$ radicals, increases [79].

In contrast, for low-concentration dye solutions, the opposite effect is observed, as the solution becomes easier to attack by $OH^{\bullet}$ radicals. It is also claimed that, for a high initial dye concentration, the amount of catalyst required for efficient degradation is also greater. Consequently, for the same oxidation time with a constant amount of catalyst, the number of $OH^{\bullet}$ radicals regenerated in the solution remains constant and does not increase. Consequently, the stable number of $OH^{\bullet}$ radicals attacking the dye molecules becomes insufficient for oxidation due to

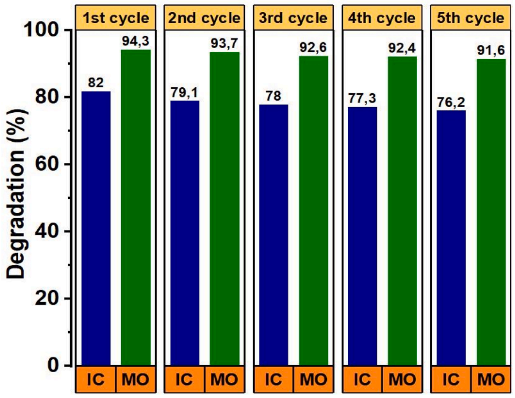

Fig. 17. Catalytic performance test of the catalyst for five oxidation test cycles of dyes.

the excessive increase in the concentration of organic matter in the dye solution [80]. Thus, optimization of the concentration of oxidizing agent (H_2O_2) and $P_2W_{17}Co$ catalyst is crucial to achieve high degradation efficiency.

The results obtained with the homogeneous Co-POM/H_2O_2 system show a clearly superior efficiency for the degradation of anionic and cationic dyes. These performances are particularly satisfactory when compared with those of innovative heterogeneous systems reported in other studies [49,81].

3.2.1.5. Effect of temperature. To examine the effect of temperature on the degradation of indigo carmine (IC) and methyl orange (MO) by H_2O_2 using (Co-POM) as catalyst, a series of experiments was carried out under the same operating conditions as above (pH = 3, [H_2O_2] = 0.154 M, [Co-POM]=0.3 mM) at temperatures ranging from 25 to 60 °C.

According to (Fig. 10), increasing temperature significantly improved reaction kinetics, manifested by an increase in oxidation rate. However, this effect was not as marked on the overall degradation efficiency, which increased from 81.95 % to 87.4 % for CI and from 94.31 % to 98.24 % for MO, for increasing temperatures from 25 °C to 60 °C respectively.

These results are in line with the literature [82], which reports that increasing temperature in the reaction medium increases the mobility of molecules, thus increasing the probability of collision between pollutant molecules and $OH^\bullet$ oxidizing species. This collision leads to a significant acceleration in reaction kinetics.

In general, higher temperatures increase the reaction rate associated with the activation of H_2O_2 by the catalyst, which logically leads to an increase in the rate of production of $OH^\bullet$ oxidizing species [83]. However, as increasing temperature does not lead to a significant improvement in degradation efficiency, and for economic reasons, ambient temperature (25 °C) was considered thereafter.

3.2.2. *Effect of the catalyst type*

The nature of the catalyst used plays a crucial role in the success of the catalytic cycle, and hence selecting the most appropriate one is essential to maximize the production of $OH^\bullet$ hydroxyl radicals [84].

Under the same operating conditions, a series of synthesized M-POMs, containing transition metals such as (Co, Cu, Ni, and Mo) (Fig. 11), were examined as catalysts for the degradation of indigo carmine (IC) and methyl orange (MO) by H_2O_2.

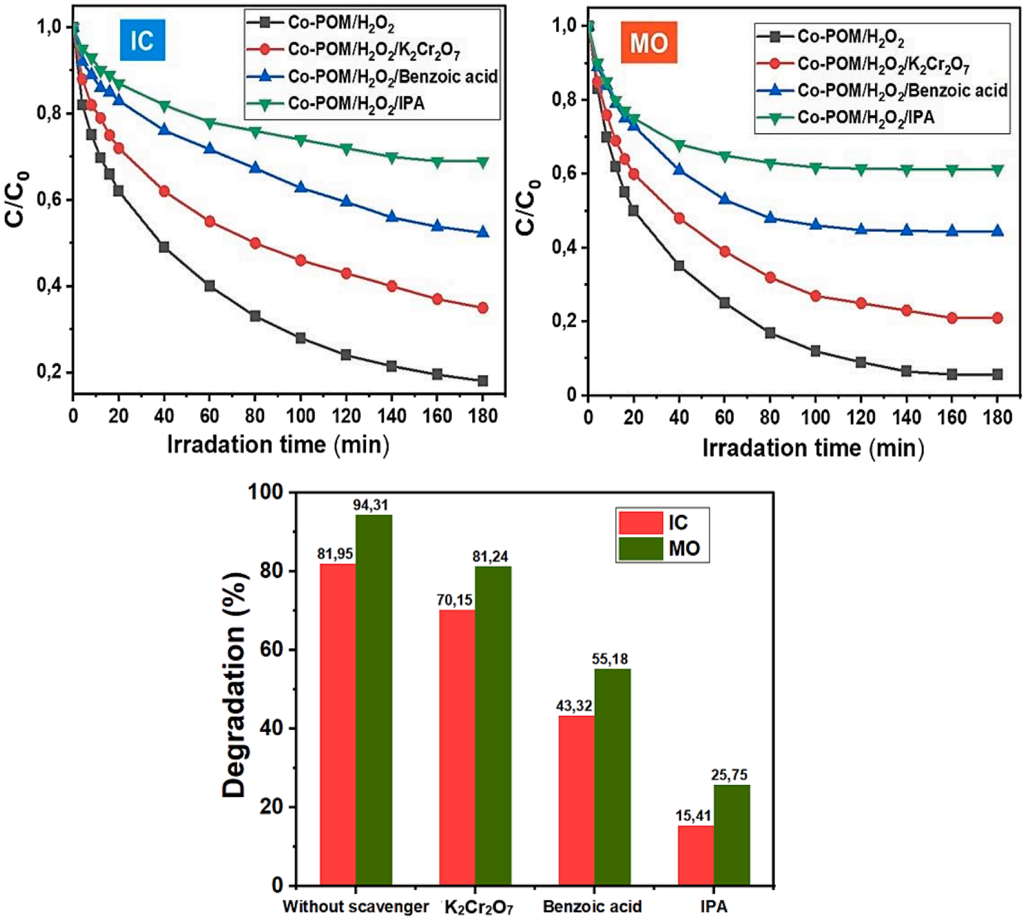

Fig. 18. Degradation as a function of irradiation time during scavenger test and their resultant efficiency for IC and MO dyes.

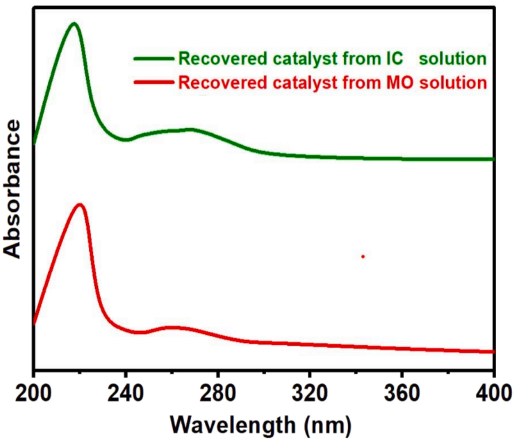

Fig. 19. UV–vis spectra of recovered catalyst after five test cycles.

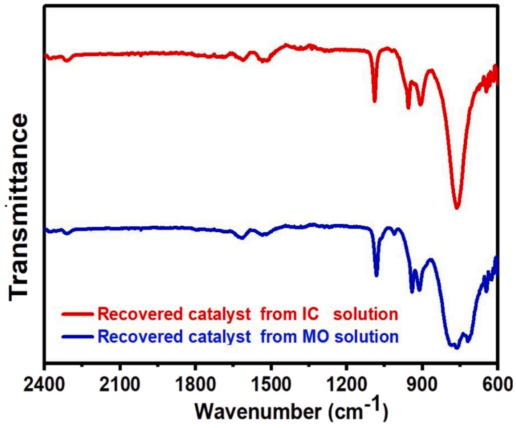

Fig. 20. Infra-red spectrums of recovered catalyst after five test cycles.

Table 5
IR vibration frequencies of recovered catalyst.

	Bandes IR (cm^{-1})			
recovered Catalyst	νas(P–O$_a$)	νas(M–O$_d$)	νas(M–O$_b$–M)	νas(M–O$_c$–M)
From IC solution	1080	953	912	756
From MO solution	1088	949	910	758

Oxidation of IC and MO by H_2O_2 in the presence of the saturated salt αP_2W_{18} showed relatively low efficiency. However, the introduction of different transition metal-containing substituted POM catalysts led to a clear improvement in the degradation efficiency of both dyes. This confirms the importance of POM catalysts in the degradation process.

Among the catalysts tested, our previously used Co-POM catalyst showed the best efficiency under these operating conditions for both dyes. These results are consistent with the related literature [85], which indicate that POMs in saturated salt form are generally less efficient for the oxidation of organic compounds than substituted forms.

The presence of the W-O-Co band in POMs catalysts enables saturated and lacunar compounds to be activated more effectively than catalysts with W-O-W bonds, thus contributing to better catalytic performance.

3.2.3. *Effect of inorganic ions*

It is well known that polluted water can contain inorganic ions such as chlorides Cl^- and sulfates SO_4^{2-} in varying concentrations, which can influence the treatment process. The effect of these ions on the degradation process logically depends on each ion, while also taking into account the behavior of the catalyst used, $P_2W_{17}Co$, with respect to these inorganic ions.

3.2.3.1. Effect of chloride ions. According to (Fig. 12), the presence of chloride ions had a significant inhibitory effect on the oxidation reaction of both dyes, resulting in a decrease in degradation efficiency. The results obtained in the presence of NaCl, $MgCl_2$ and $CaCl_2$ ions were 40.96 %, 78.05 % and 64.39 % respectively for IC, and 72.14 %, 84.21 % and 87.52 % for MO. The inhibition of the degradation reaction by chloride ions can be explained by the blocking of active catalyst sites and/or by competition between chloride ions and pollutant molecules to react with the $OH^{\bullet}$ radicals generated.

Indeed, it has been reported that chloride ions capture oxidizing radical species. This phenomenon is explained by the reaction of $OH^{\bullet}$ radicals with Cl^- ions, which leads to the formation of inorganic radicals such as $Cl^{\bullet}$ and $HClO^{\bullet}$ according to the following reactions [86]:

$$Cl^- + OH^{\bullet} \rightarrow ClO^{\bullet} + OH^- \tag{9}$$

$$Cl^- + OH^{\bullet} \rightarrow HClO^{\bullet} \tag{10}$$

These radicals, although in principle capable of oxidizing organic pollutants and participating in the degradation process, are however less reactive with organic matter than $OH^{\bullet}$ radicals [87]. However, the generation of $Cl^{\bullet}$ radicals plays a major role in the formation of chlorinated organic compounds, known to be particularly harmful intermediate substances.

Moreover, in acidic conditions, it is highly likely that the $Cl_2^{\bullet}$ dichloride radical is formed by reaction between the added Cl^- ions and the $Cl^{\bullet}$ radicals produced (Eq 11), or with the $OH^{\bullet}$ radicals generated (Eq 12). This radical ($E_0 = 1.36$ eV) is also less reactive than the $OH^{\bullet}$ radical [88].

$$Cl^{\bullet} + Cl^- \rightarrow Cl_2^{\bullet} \tag{11}$$

$$2Cl^- + OH^{\bullet} + H^+ \rightarrow Cl_2^{\bullet} + H_2O \tag{12}$$

3.2.3.2. Effect of sulfate ions. According to (Fig. 13), the presence of sulfate ions does not significantly affect degradation efficiency. For Na_2SO_4, MgSO4, and $CaSO_4$ ions, the yields obtained were 80.97 %, 77.61 %, and 78.5 % for indigo carmine (IC), and 90.06 %, 91.12 %, and 83.31 % for methyl orange (MO), respectively. However, there was a noticeable slowdown in reaction kinetics.

This can be explained by the adsorption of sulfate ions on the catalyst surface, which disrupts the proper functioning of certain active sites [89].

In parallel, the stability of the degradation efficiency could be explained by the reaction of sulfate ions with $OH^{\bullet}$ radicals, leading to the formation of the sulfate radical ($SO_4^{\bullet}$) according to the following equation:

$$SO_4^{2-} + OH^{\bullet} \rightarrow SO_4^{-\bullet} + OH^- \tag{13}$$

Then, the ($SO_4^{-\bullet}$) radical can react with the water molecule to produce more SO_4^{2-} and $OH^{\bullet}$ ions as follows [90]:

$$SO_4^{-\bullet} + H_2O \rightarrow SO_4^{2-} + OH^{\bullet} + H^+ \tag{14}$$

The sulfate radical ($SO_4^{-\bullet}$) formed is a powerful oxidant ($E_0 = 2.6$ eV), which participates in reactions with organic compounds [88]. This explains the continuation of the oxidation effect even after the time required to reach final stabilization (180 min). However, this activity is accompanied by a slowdown in reaction rate, due to disruption of the catalyst's active sites and a disturbance in the $OH^{\bullet}$ radical production cycle, affecting their oxidative role.

3.2.4. *UV–vis absorbance spectra of dye before and after oxidation*

The oxidation reaction of indigo carmine (IC) and methyl orange

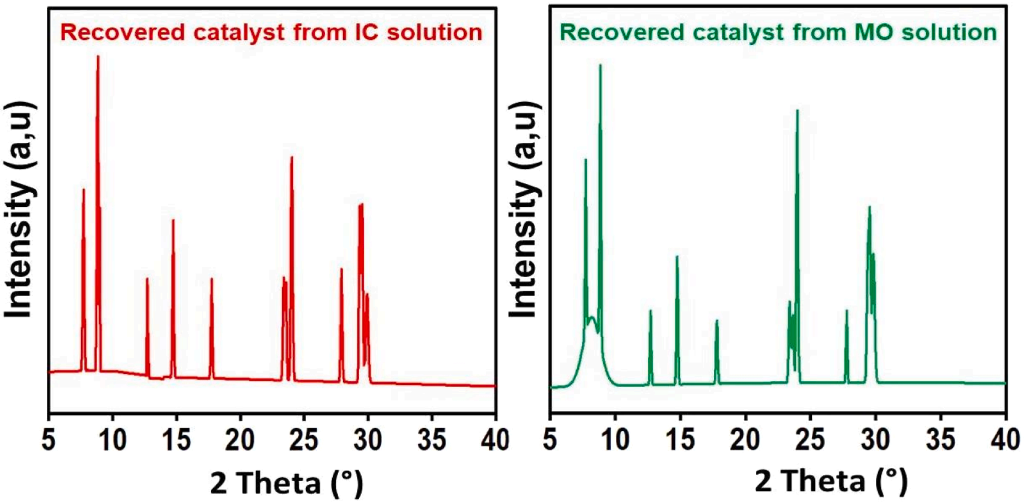

Fig. 21. Powder X-ray diffraction patterns of recovered catalyst after five test cycles.

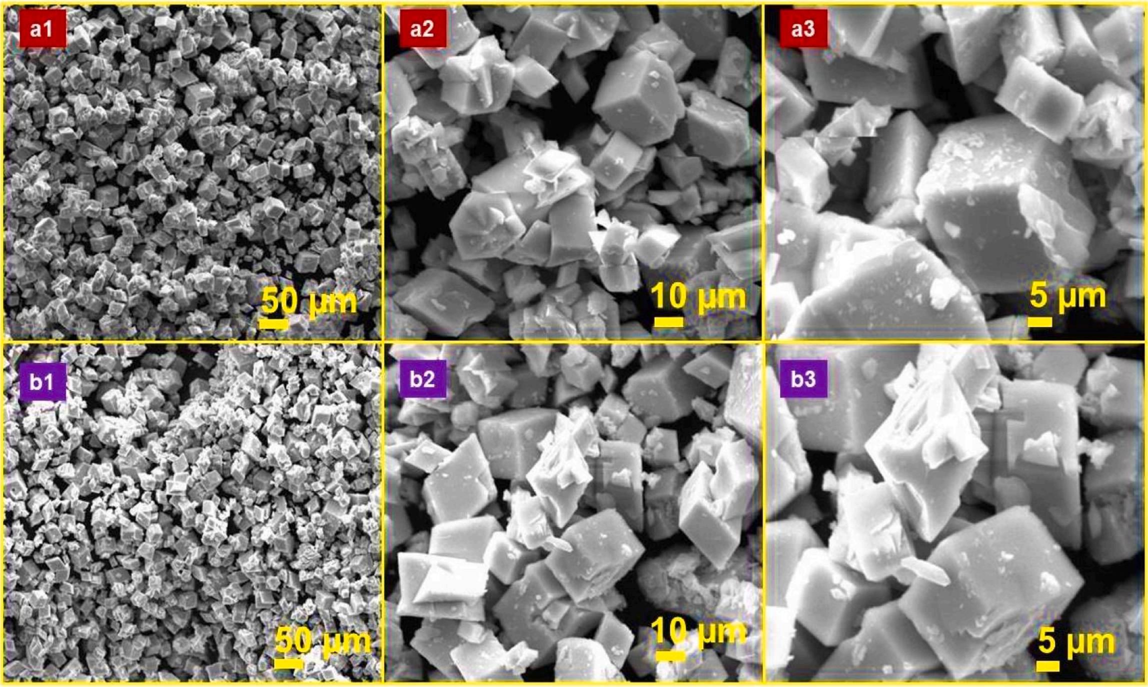

Fig. 22. FE-SEM photographs of recovered catalyst after five test cycle at different magnifications: (a) recovered from IC solution; (b) recovered from MO solution.

(MO) by the homogeneous ($H_2O_2/P_2W_{17}Co$) system was carried out under optimum conditions, tracking the spectral evolution as a function of time by UV-visible spectrophotometry in a wavelength range from 200 to 800 nm. (Fig. 14) shows the spectral evolution of the two dyes over the 180 min oxidation period.

The spectra show that the disappearance of IC and MO by the homogeneous (H_2O_2/Co-POM) system was confirmed, as the appearance of the spectra after 180 min was different from that observed before the addition of the H_2O_2 oxidizing agent.

For indigo carmine, and according to similar studies on the oxidation of this dye [91], the process begins with an attack of $OH^\bullet$ radicals at the C(1) and C(10) positions of the structure, resulting in the disruption of the indigoid C═C band ($\lambda_{max} = 611$ nm), producing isatin sulfonic acid ($\lambda = 244$ nm) as the main aromatic intermediate.

For orange methyl, the first stage of the oxidation process involves the progressive disruption of the N═N azo band ($\lambda_{max} = 506$ nm) by H_2O_2, as illustrated in (Fig. 14). This progressive breakdown in the visible region is accompanied by an increase in the absorption band in the UV region ($\lambda = 270$ nm), corresponding to the benzene ring, indicating the conversion of oxidized MO to aromatic intermediates [92]. The decrease in the indigoid and azo bands, accompanied by a gradual disappearance of color over time, testifies to the strong reactivity of H_2O_2 towards these dyes. This reactivity is represented by the destruction of the C═C and N═N functional groups responsible for the color, without the appearance of new absorption bands in this region.

3.2.5. Oxidation mechanism of IC and MO dyes

Several metals, particularly transition metals, are capable of initiating hydrogen peroxide decomposition to generate $OH^\bullet$ hydroxyl radicals [82]. For cobalt (Co^{II}), the hydrogen peroxide decomposition reaction is written as follows:

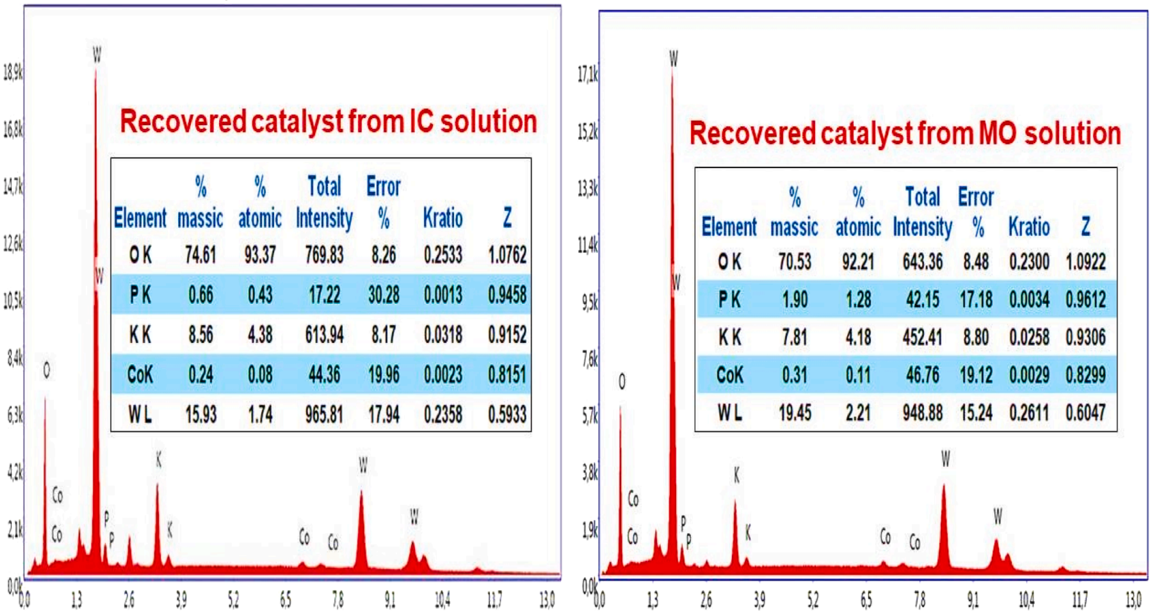

Recovered catalyst from IC solution

Element	% massic	% atomic	Total Intensity	Error %	Kratio	Z
O K	74.61	93.37	769.83	8.26	0.2533	1.0762
P K	0.66	0.43	17.22	30.28	0.0013	0.9458
K K	8.56	4.38	613.94	8.17	0.0318	0.9152
CoK	0.24	0.08	44.36	19.96	0.0023	0.8151
W L	15.93	1.74	965.81	17.94	0.2358	0.5933

Recovered catalyst from MO solution

Element	% massic	% atomic	Total Intensity	Error %	Kratio	Z
O K	70.53	92.21	643.36	8.48	0.2300	1.0922
P K	1.90	1.28	42.15	17.18	0.0034	0.9612
K K	7.81	4.18	452.41	8.80	0.0258	0.9306
CoK	0.31	0.11	46.76	19.12	0.0029	0.8299
W L	19.45	2.21	948.88	15.24	0.2611	0.6047

Fig. 23. EDX spectra of recovered catalyst after five test cycles.

$$Co^{2+} + H_2O_2 \rightarrow Co^{3+} + OH^{-} + OH^{\bullet} \tag{15}$$

The action of H_2O_2 on a complex containing the Co(II) ion leads to the release of $OH^{\bullet}$ radicals, but also $HO_2^{\bullet}$, which also participate in the oxidation of the dye. For our Co-POM cobalt-substituted catalyst, (path 1) in the mechanism shown in (Fig. 15) can be considered.

Also, it has been reported that the presence of the oxidant H_2O_2 in the presence of POMs can lead to the formation of peroxo-POM complexes [93], which are powerful oxidants capable of oxidizing organic compounds by direct oxygen transfer (path 2) or by the superoxydes ($O_2\bullet$) generated from the peroxo-complex, depending on (path 3) in the oxidation mechanism (Fig. 15).

3.2.6. *Catalyst activity and stability*

The industrial application of a catalyst and its cost-effectiveness depend to a large extent on its stability. One of the advantages of homogeneous polyoxometalate catalysis is that the catalyst can be easily recovered and reused several times [37], which is a major economic advantage. To verify the stability and catalytic performance of Co-POM, we recovered it after each cycle by gradually adding KCl to the colored solution until the formation of a precipitate (Fig. 16). The resulting precipitate was then washed and dried at room temperature (25 °C) for sufficient time to remove any water or organic molecules, then reused. The recycling efficiency test is displayed in (Fig. 17), showing that the activity and stability of Co-POM are clearly verified, since for both dyes it retained almost the same catalytic performance even after several oxidation cycles with hydrogen peroxide (H_2O_2). The slight decrease in efficiency observed was logically due to the loss of mass during the recycling process.

3.2.7. *Scavenger test*

A trapping test was carried out to identify the active chemical species responsible for, or the main contributor to, dye degradation. This test provides a better understanding of the mechanism underlying the catalytic oxidation process. To this end, specific trapping agents were added separately: isopropanol (IPA) to trap hydroxyl radicals ($OH^{\bullet}$), potassium dichromate ($K_2Cr_2O_7$) for superoxides ($O_2^{\bullet}$), and benzoic acid ($C_7H_6O_2$) for hydroperoxyl radicals ($HO_2^{\bullet}$).According to the test results shown in (Fig. 18), $OH^{\bullet}$ radicals are the main contributors to oxidation activity. In contrast, ($O_2^{\bullet}$) and ($HO_2^{\bullet}$) have a relatively limited impact. In the presence of the Co-POM metal nanocomposite, the addition of IPA to the dye solution results in a significant reduction in degradation. These observations are in line with numerous studies [94–97], which demonstrate that ($OH^{\bullet}$) radicals play a predominant role in the degradation of various dyes, surpassing the effect of other reactive species.

3.3. *Characterization of recovered catalyst*

To confirm the stability of the Co-POM structure, after the fifth cycle characterizations using the analytical techniques used in the previous study were performed [45], namely UV–Vis, FT-IR, DRX and SEM-EDX spectroscopy.

3.3.1. *UV–Visible spectroscopy*

As shown in the (Fig. 19), after five oxidation cycles using H_2O_2, the UV–Vis spectra of the recovered catalyst remained unchanged from those of the initial catalyst. They still displayed two main peaks, located around 220 nm and 270 nm, corresponding to the π-d electronic transitions of the (Od→M) and (Ob/Oc→M) bands, respectively [45,98].

3.3.2. *FT-IR Spectroscopy*

(Fig. 20) shows the IR spectra of $P_2W_{17}Co$ after five cycles of oxidation of the IC and MO dyes with H_2O_2 and the observed vibrational bands are summarized in (Table 5), showing that all the characteristic bands of the Dawson structure were present in the spectra of the recovered catalyst, always in the region of 700 to 1100 cm^{-1} [33,45].

3.3.3. *X-ray diffraction (XRD)*

The catalyst recovered after five cycles of H_2O_2 oxidation of the IC and MO dyes was analyzed by X-ray diffraction (Fig. 21), showing that the principal 2θ diffraction angles remain consistent with the Dawson structure [37,45]. Indeed, characteristic peaks were observed at the following angles: 7°–10°, 17°–20°, 23°–28°, and 28°–30°.

3.3.4. *SEM-EDX*

(Fig. 22) reveals that there was no significant change in the morphology and microstructure of the catalyst after five cycles of use, owing to the similarity of the SEM images between the recovered catalyst and the initial one. It can be seen that the majority of the grains display a cubic or pseudo-cubic shape, with heterogeneous sizes, without any apparent modification.

The EDX spectrograms in (Fig. 23) of the recovered catalysts confirmed the results obtained, due to the presence of the same elements (P, O, K and W) as in the initial catalyst. The high proportions of tungsten (W) and oxygen (O) indicated a chemical composition consistent with that of the catalyst prior to its use.

4. Conclusion

In the present study, Wells-Dawson polyoxometalate nanoparticles K_6-$[\alpha P_2W_{18}O_{62}]^{6-}$ and K_6-$[P_2W_{17}O_{61}]^{10-}$ were prepared by facile synthesis, resulting in an environmental material K_8-$[\alpha_2P_2W_{17}O_{61}Co]^{8-}$. The latter was used as a homogeneous catalyst for the degradation of the toxic dyes IC and MO in aqueous solution by H_2O_2. These metal complexes were characterized by X-ray diffraction (XRD), scanning electron microscopy (SEM) and elemental analysis of chemical composition. These characterizations showed that the metal element Co(II) tends to fill the gap of monolacunar (P_2W_{17}), leading to the saturated Co-POM species with a pure, well-defined Wells-Dawson structure.

The degradation study shows conclusively that the use of Co-POM nanoparticles for water depollution is technically feasible, environmentally friendly and economically attractive. Separate oxidation of MO and IC by H_2O_2 in the presence of the Co-POM catalyst confirmed the reactivity of H_2O_2 towards these organic pollutants, with a very high degradation rate (ED = 87.4 % for IC and ED = 94.31 % for MO).

Catalyst recycling confirmed the catalytic performance of Co-POM, as evidenced by high degradation efficiencies even after five cycles of use. The stability and robustness of this catalyst recovered after the fifth cycle were also confirmed by the FT-IR, UV–vis, XRD, FE-SEM and EDX analytical methods used in our previous study [45]. The new homogeneous catalyst system (H_2O_2/Co-POM/Dye) used in this study can be considered a promising and cost-effective environmental alternative for the treatment of toxic organic pollutants in wastewater.

CRediT authorship contribution statement

Mohammed Grabsi: Writing – review & editing, Writing – original draft, Validation, Supervision, Data curation. **Nacéra Zabat:** Project administration, Methodology. **Mohamed Djermane:** Software, Methodology. **Abdeltif Amrane:** Writing – review & editing.

Declaration of competing interest

No competing Interest.

Acknowledgments

The authors thank the Ministry of Higher Education and Scientific Research, Algeria for the financial support through the PRFU project (N°: A16N01UN230120230001).

Data availability

No data was used for the research described in the article.

References

[1] S. Amirahmadi, O. Moradi, S. Arab-Salmanabadi, The adsorption of direct red 23 as a toxic pollutant in aqueous solution by using surface modified metal-organic framework containing tricarboxylic acid benzene ligand, Desalin. Water Treat. 317 (2024) 100132, https://doi.org/10.1016/j.dwt.2024.100132.

[2] N. Behzad, O. Moradi, H. Raissi, M. Hakimi, S. Mozaffari, Synthesis of graphene oxide–magnesium oxide composites and cationic dyes removal from water, Desalin. Water Treat. 300 (2023) 213–229, https://doi.org/10.5004/dwt.2023.29728.

[3] J. Khodayari, K. Zare, O. Moradi, M. Kalaee, N.M. Mahmoodi, Synthesis of eco-friendly carboxymethyl cellulose /metal–organic framework biocomposite and its photocatalytic activity, J. Photochem. Photobiol. Chem. 446 (2023) 115097, https://doi.org/10.1016/j.jphotochem.2023.115097.

[4] O. Moradi, I.D. Sharabaf, Separation of organic contaminant (dye) using the modified porous metal-organic framework (MIL), Environ. Res. 214 (2022) 114006, https://doi.org/10.1016/j.envres.2022.114006.

[5] J. Yang, C. Wu, H. Fang, X. Chen, J. Lv, Exploring the requirements of reactive dyes in eco-friendly dyeing process: the relationship between dye structure, dyeing properties, and eco-friendly dyeing techniques, Dyes Pigm. 223 (2024) 111976, https://doi.org/10.1016/j.dyepig.2024.111976.

[6] S. Adeel, S. Abrar, M. Ozomay, N. Fazal-Ur-Rehman, M. Hussaan, F. Batool, Evolving role of plant pigments in the cosmetic industry, Elsevier eBooks (2024) 307–319, https://doi.org/10.1016/b978-0-443-15213-9.00014-4.

[7] Md.A.A. Fahad, R. Ahamed, T. Ahmed, N. Jahan, R. Mia, G.F.I. Toki, S.T. Mahmud, K.K. Niloy, Pharmaceutical Applications of Natural Dyes and Pigments, Elsevier eBooks, 2024, pp. 165–175, https://doi.org/10.1016/b978-0-443-15213-9.00011-9.

[8] M.E.M. Soutelino, G. De Paiva Vieira, M.B. Goulart, K.C. Miranda, R.P. Da Conceição, T.C. Pimentel, A.G. Da Cruz, R. Da Silva Rocha, Natural food dyes on dairy products: A critical approach between 2012-2023 literature regarding the technological and functional aspects, health benefits and future trends, Trends Food Sci. Technol. (2024) 104370, https://doi.org/10.1016/j.tifs.2024.104370.

[9] Md.R. Repon, B. Dev, M.A. Rahman, S. Jurkonienė, A. Haji, Md.A. Alim, E. Kumpikaitė, Textile dyeing using natural mordants and dyes: a review, Environ. Chem. Lett. 22 (2024) 1473–1520, https://doi.org/10.1007/s10311-024-01716-4.

[10] O. Moradi, S. Panahandeh, Fabrication of different adsorbents based on zirconium oxide, graphene oxide, and dextrin for removal of green malachite dye from aqueous solutions, Environ. Res. 214 (2022) 114042, https://doi.org/10.1016/j.envres.2022.114042.

[11] O. Moradi, A.H. Naeini, M.R. Kalaee, S.M.R. Mirkhan, The effect of sustainable applications of chitin and chitosan to remove dyed pollutants using adsorption: a review, NANO 18 (2023) 2330006, https://doi.org/10.1142/s1793292023300062.

[12] O. Moradi, G. Sharma, Emerging novel polymeric adsorbents for removing dyes from wastewater: A comprehensive review and comparison with other adsorbents, Environ. Res. 201 (2021) 111534, https://doi.org/10.1016/j.envres.2021.111534.

[13] X. Li, H. Liu, Y. Zhang, J. Mahlknecht, C. Wang, A review of metallurgical slags as catalysts in advanced oxidation processes for removal of refractory organic pollutants in wastewater, J. Environ. Manage. 352 (2024) 120051, https://doi.org/10.1016/j.jenvman.2024.120051.

[14] I.H. Anyaene, O.D. Onukwuli, A.K. Babayemi, I.A. Obiora-Okafo, E.M. Ezeh, Application of bio coagulation–Flocculation and soft computing aids for the removal of organic pollutants in aquaculture effluent discharge, Chem. Africa 7 (2023) 455–478, https://doi.org/10.1007/s42250-023-00754-9.

[15] S.M. Samianifard, M. Kalaee, O. Moradi, N.M. Mahmoodi, D. Zaarei, Synthesis of novel starch/zeolitic imidazolate framework (ZIF-67)/graphene oxide biocomposite and photocatalytic dye degradation ability, Opt. Mater. 151 (2024) 115268, https://doi.org/10.1016/j.optmat.2024.115268.

[16] S.M. Samianifard, M. Kalaee, O. Moradi, N.M. Mahmoodi, D. Zaarei, Novel biocomposite (Starch/metal–organic framework /Graphene oxide): synthesis, characterization and visible light assisted dye degradation, J. Photochem. Photobiol. Chem. 450 (2023) 115417, https://doi.org/10.1016/j.jphotochem.2023.115417.

[17] R. Sumethra, T. Jayakumari, P. Gayathri, K. Ravichandran, M. Varshini, C. Jenipher, M. Ayyanar, An ecofriendly approach for the synthesis of Ni/NiO/g-C3N4 nanocomposite using Cleome gynandra leaf extract for biomedical and photocatalytic applications, NANO (2024), https://doi.org/10.1142/s1793292024500930.

[18] K. Ravichandran, R. Shalini, M. Ayyanar, P. Kavitha, M. Baneto, M. Karunakaran, P.K. Praseetha, K.C.S. Pushpa, N. Anuradha, Effect of pH of the precursor solution on the photocatalytic and biomedical applications of enzyme coupled ZnO and SnO2 nanomaterials: a comparative study, J. Water Process Eng. 53 (2023) 103817, https://doi.org/10.1016/j.jwpe.2023.103817.

[19] K. Ravichandran, S. Suvathi, P. Kavitha, B. Kaleeswaran, M. Vasuki, G. Mahalakshmi, M. Ayyanar, Photocatalytic dye decomposition by bio-enzyme enriched TiO2/g-C3N4 nanocomposite and assessment of toxicity of resultant water using Catla catla fish, Biocatal. Agric. Biotechnol. 58 (2024) 103135, https://doi.org/10.1016/j.bcab.2024.103135.

[20] B. Farahani, M. Giahi, M.H. Ghorbani, R. Fazaeli, O. Moradi, Synthesis of CuS/NiS heterostructural photocatalyst and its performance in the degradation of metronidazole and diclofenac drugs: optimization of operating conditions, J. Nanostr. Chem. 13 (2023) 303–320, https://doi.org/10.1007/s40097-022-00520-2.

[21] P.S. Chauhan, K. Singh, A. Choudhary, U. Brighu, S.K. Singh, S. Bhattacharya, Combined advanced oxidation dye-wastewater treatment plant: design and development with data-driven predictive performance modeling, Npj Clean Water 7 (2024), https://doi.org/10.1038/s41545-024-00308-7.

[22] E. Wang, Y. Shang, F. Li, M. Xiao, S. Yan, Organic-inorganic composite membrane-based transport membrane condenser: performance of waste recovery from hot gas mixture of CO2 and water vapor, Sep. Purif. Technol. 330 (2024) 125306, https://doi.org/10.1016/j.seppur.2023.125306.

[23] M. Khalid, Y. Park, R.R. Karri, R. Walvekar, Advanced oxidation processes for micropollutant remediation, 2023. https://doi.org/10.1201/9781003247913.

[24] M. Rabieian, F. Qaderi, Optimizing hybrid photocatalytic-ozonation for offshore produced water treatment, J. Shahroodut. Ac. Ir (2024), https://doi.org/10.22044/jme.2023.13081.2376.

[25] K.A.S. Arasu, A.G. Raja, R. Rajaram, Photocatalysis and antimicrobial activity of ZnO@TiO 2 core-shell nanoparticles, Inorganic Nano-Metal Chem. (2024) 1–12, https://doi.org/10.1080/24701556.2024.2353742.

[26] A. Dehane, S. Merouani, Chapter 20 challenges and prospects of the sonochemical process, De Gruyter eBooks (2024) 467–480, https://doi.org/10.1515/9783111137940-020.

[27] H. Yu, Y. He, H. Tao, H. Yuan, F. Wu, R. Zou, S. Xu, L. Gu, Insight into simultaneously sludge dewatering and antiviral drugs removal by integrated particle electrodes assisted electrochemical oxidation, J. Environ. Chem. Eng. 12 (2024) 113899, https://doi.org/10.1016/j.jece.2024.113899.

[28] H. Targhan, A. Rezaei, A. Aliabadi, A. Ramazani, Z. Zhao, H. Zheng, Palladium-based pseudohomogeneous catalyst for highly selective aerobic oxidation of benzylic alcohols to aldehydes, Sci. Rep. 14 (2024), https://doi.org/10.1038/s41598-023-49526-y.

[29] Z. Song, L. Liu, X. Zhu, Z. Ren, J. Bai, Cobalt-based catalysts for catalytic oxidation of biomass-derived 5-hydromethylfurfural to value-added chemicals, Renew. Sustainable Energy Rev. 189 (2024) 114003, https://doi.org/10.1016/j.rser.2023.114003.

[30] N. Mizuno, K. Yamaguchi, K. Kamata, Y. Nakagawa, Activation of hydrogen peroxide by polyoxometalates, Elsevier eBooks (2008) 155–176, https://doi.org/10.1016/b978-0-444-53188-9.00004-3.

[31] W.A. Shah, S.M. Abbas, M. Adil, S. Ibrahim, Q.A. Bhatti, S. Li, Catalytic efficiency and kinetic analysis of manganese polyoxometalate heterogenized in MIL-100-Fe for selective olefin oxidation using H2O2, Molec. Catal. 567 (2024) 114456, https://doi.org/10.1016/j.mcat.2024.114456.

[32] O.V. Zalomaeva, N.V. Maksimchuk, S.M. Marikovskaya, A.A. Antonov, O. A. Kholdeeva, Highly selective thioether oxidation with H2O2 catalyzed by Zr-substituted keggin phosphotungstate: mechanistic insights, Chem. Cat. Chem. 16 (2023), https://doi.org/10.1002/cctc.202301374.

[33] N. Zabat, Green complexation for removal of Ni2+ from synthetic effluents by a nanomaterial polyoxometalate, Current Res. Green Sustain. Chem. 5 (2022) 100243, https://doi.org/10.1016/j.crgsc.2021.100243.

[34] N. Zabat, Synthesis of eco-friendly nanocomposite polyoxometalates Dawson type and their application for the removal of cadmium from aqueous solution, Nanotechnol. Environ. Eng. 7 (2022) 209–222, https://doi.org/10.1007/s41204-022-00215-7.

[35] N. Zabat, Removal of lead by complexation using a heteropolyanion and extraction of formed complex by emulsified liquid membrane, J. Environ. Chem. Eng. 5 (2017) 2018–2023, https://doi.org/10.1016/j.jece.2017.03.042.

[36] I.K. Song, M.A. Barteau, Correlation of negative differential resistance (NDR) peak voltages of nanostructured heteropolyacid (HPA) monolayers with one electron reduction potentials of HPA catalysts, Langmuir 20 (2004) 1850–1855, https://doi.org/10.1021/la030281z.

[37] N. Zabat, Nickel-substituted polyoxometalate nanomaterial as a green and recyclable catalyst for dye decolorization, Arabian J. Sci. Eng. 44 (2018) 227–236, https://doi.org/10.1007/s13369-018-3503-9.

[38] N. Zabat, M. Abbessi, Study of simultaneous complexation of heavy metals by a mixed heteropolyanion of dawson type, Desalin. Water Treat. 53 (2013) 709–717, https://doi.org/10.1080/19443994.2013.848653.

[39] Z. Nacéra, Comparative study of discoloration of mono-azo dye by catalytic oxidation based on wells-dawson heteropolyanion catalyst, Environ. Nanotechnol. Monitor. Manag. 10 (2018) 10–16, https://doi.org/10.1016/j.enmm.2018.04.003.

[40] N. Zabat, M. Abbessi, Elimination of the methyl blue from wastewater by advanced oxidation process in the presence of an heteropolyanion of Dawson type as a catalyst, Res. Chem. Intermed. 41 (2013) 1691–1702, https://doi.org/10.1007/s11164-013-1304-z.

[41] N. Zabat, M. Grabsi, I. Harbi, Elimination of an organic pollutant from wastewater by a chemical oxidation process catalyzed by a Nano-polyoxometalate of Dawson type, 2 (2019). https://doi.org/10.48393/imist.prsm/jases-v2i4.18529.

[42] R. Contant, J.-P. Ciabrini, Stereospecific preparations of new n-molybdo-(18-n)-tungsto-2-phosphates and related "defect" compounds (n = 2, 4 or 5), J. Inorg. Nucl. Chem. 43 (1981) 1525–1528, https://doi.org/10.1016/0022-1902(81)80330-2.

[43] M. Abbessi, R. Contant, R. Thouvenot, G. Herve, Dawson type heteropolyanions. 1. Multinuclear (phosphorus-31, vanadium-51, tungsten-183) NMR structural investigations of octadeca(molybdotungstovanado)diphosphates .Alpha.-1,2,3-[P2MM'2W15O62]n- (M, M' = Mo, V, W): syntheses of new related compounds, Inorg. Chem. 30 (1991) 1695–1702, https://doi.org/10.1021/ic00008a006.

[44] R. Contant, M. Abbessi, R. Thouvenot, G. Hervé, Dawson type heteropolyanions. 3. Syntheses and31P,51V, and183W NMR structural investigation of octadeca (molybdo-tungsto-vanado)diphosphates related to the [H2P2W12O48]12-anion, Inorg. Chem. 43 (2004) 3597–3604, https://doi.org/10.1021/ic049885w.

[45] M. Grabsi, N. Zabat, N. Khellaf, F. Ismail, Synthesis of an environmental nano-polyoxometalate (α2P2W17CoO61)8− as catalyst for dyes degradation: a comparative study oxidation of indigoid and azo dyes, Environ. Nanotechnol. Monitor. Manag. 12 (2019) 100269, https://doi.org/10.1016/j.enmm.2019.100269.

[46] O. Ozalp, F. Oguz, M. Soylak, Activated carbon from green walnut shells as the adsorbent for the solid-phase extraction of indigo carmine from food and textiles, Instrumentation Sci. Technol. (2024) 1–15, https://doi.org/10.1080/10739149.2024.2368190.

[47] M.K. Zadeh, O. Moradi, S. Arab-Salmanabadi, A study on the novel use of metal-organic frameworks (MOFs) as a nanocomposite of MIL-88A(FE) for the photocatalytic degradation of azo dyes from aqueous solutions: synthesis and characterization, Chem. Select 9 (2024), https://doi.org/10.1002/slct.202404797.

[48] O. Moradi, M. Mirzaian, S. Sedaghat, Poly(methyl methacrylate) functionalized graphene oxide/CuO as nanocomposite for efficient removal of dye pollutants, Sci. Rep. 14 (2024) 22318, https://doi.org/10.1038/s41598-024-72937-4.

[49] O. Moradi, A. Pudineh, S. Sedaghat, Synthesis and characterization Agar/GO/ZnO NPs nanocomposite for removal of methylene blue and methyl orange as azo dyes from food industrial effluents, Food Chem. Toxicol. 169 (2022) 113412, https://doi.org/10.1016/j.fct.2022.113412.

[50] R. Contant. J. P. Ciabrini, Préparation et propriétés des solutions de quelques hétéropolyanions lacunaires dérivés des 18-tungsto-2-phosphates (isomères α et β), J. Chem. Res 222 (1977) 2601–2609.

[51] R. Massart, R. Contant, J.M. Fruchart, J.P. Ciabrini, M. Fournier, Phosphorus-31 NMR studies on molybdic and tungstic heteropolyanions. Correlation between structure and chemical shift, Inorg. Chem. 16 (1977) 2916–2921, https://doi.org/10.1021/ic50177a049.

[52] J. Bartis, M. Dankova, J.J. Lessmann, Q.-H. Luo, W.DeW. Horrocks, L. C. Francesconi, Lanthanide complexes of the α-1 isomer of the [P2W17O61]10-heteropolytungstate: preparation, stoichiometry, and structural characterization by183W and31P NMR spectroscopy and europium(III) luminescence spectroscopy, Inorg. Chem. 38 (1999) 1042–1053, https://doi.org/10.1021/ic980384i.

[53] P.-K. Wang, W.-F. Wang, K.-B. Jiang, B.-Y. Li, S.-H. Wang, F.-K. Zheng, G.-C. Guo, Efficient X-ray detection of polyoxometalates@metal–Organic frameworks based on host–Guest electron transfer, ACS Mater. Letters 6 (2024) 1086–1093, https://doi.org/10.1021/acsmaterialslett.3c01640.

[54] G. Liu, L. Liu, T. Gong, Y. Li, L. Chen, J. Zhao, Nicotinic-acid-ornamented tetrameric rare-earth-substituted phospho(III)tungstates with the coexistence of mixed Keggin/Dawson building blocks and its honeycomb nanofilm for detecting toxins, Inorg. Chem. 60 (2021) 14457–14466, https://doi.org/10.1021/acs.inorgchem.1c02248.

[55] İ. Küçük, S. Vural, S. Köytepe, T. Seçkin, Synthesis, characterization and dielectric properties of nickel-based polyoxometalate/polyurethane composites, Polymer-Plastics Technol. Mater. 58 (2019) 1445–1460, https://doi.org/10.1080/25740881.2018.1563123.

[56] İ. Küçük, S. Vural, N. Kılıcım, İ. Adıgüzel, S. Köytepe, T. Seçkin, Preparation of the copper-based polyoxometalate/polyurethane composites and their dielectric properties, Polym. Polym. Compos. 28 (2019) 473–483, https://doi.org/10.1177/0967391119887574.

[57] M.M. Dobson, R.J.D. Tilley, A new pseudo-binary tungsten oxide, W17O47, Acta Crystallogr., Sect. B: Struct. Sci. 44 (1988) 474–480, https://doi.org/10.1107/s0108768188004380.

[58] I.J. McColm, R. Steadman, S.J. Wilson, Iron-promoted phases in the tungsten-oxygen system, J. Solid State Chem. 23 (1978) 33–42, https://doi.org/10.1016/0022-4596(78)90051-8.

[59] M.-r. Spirlet, W.R. Busing, Dodecatungstophosphoric acid-21-water by neutron diffraction, Acta. Crystallographica Section B 34 (1978) 907–910, https://doi.org/10.1107/s0567740878004306.

[60] Arne. Magnéli, Crystal structure studies on beta-tungsten oxide, Ark. Kemi 1 (1949) 223–230.

[61] B. Dawson, The structure of the 9(18)-heteropoly anion in potassium 9(18)-tungstophosphate, K6(P2W18O62).14H2O, Acta Crystallogr. 6 (1953) 113–126, https://doi.org/10.1107/s0365110x53000466.

[62] S. Lambert, H. Leligny, D. Grebille, Three forms of the misfit layered cobaltite [Ca2CoO3] [CoO2]1.62·A 4D structural investigation, J. Solid State Chem. 160 (2001) 322–331, https://doi.org/10.1006/jssc.2001.9235.

[63] C. Suryanarayana, M.G. Norton, Practical aspects of X-ray diffraction, Springer eBooks (1998) 63–94, https://doi.org/10.1007/978-1-4899-0148-4_3.

[64] G.K. Williamson, W.H. Hall, X-ray line broadening from filed aluminium and wolfram, Acta Metall. 1 (1953) 22–31, https://doi.org/10.1016/0001-6160(53)90006-6.

[65] M. Khan, A. Mishra, J. Shukla, P. Sharma, X-ray analysis of BaTiO3 ceramics by Williamson-Hall and size strain plot methods, AIP Conf. Proc. (2019), https://doi.org/10.1063/1.5098692.

[66] L.E. Briand, G.T. Baronetti, H.J. Thomas, The state of the art on Wells–Dawson heteropoly-compounds, Appl. Catalysis a General 256 (2003) 37–50, https://doi.org/10.1016/s0926-860x(03)00387-9.

[67] S. Antonaraki, T.M. Triantis, E. Papaconstantinou, A. Hiskia, Photocatalytic degradation of lindane by polyoxometalates: intermediates and mechanistic aspects, Catal. Today 151 (2010) 119–124, https://doi.org/10.1016/j.cattod.2010.02.017.

[68] L. Szpyrkowicz, C. Juzzolino, S.N. Kaul, A comparative study on oxidation of disperse dyes by electrochemical process, ozone, hypochlorite and fenton reagent, Water Res. 35 (2001) 2129–2136, https://doi.org/10.1016/s0043-1354(00)00487-5.

[69] M. Lucas, J. Peres, Decolorization of the azo dye Reactive Black 5 by Fenton and photo-Fenton oxidation, Dyes Pigm. 71 (2006) 236–244, https://doi.org/10.1016/j.dyepig.2005.07.007.

[70] G.V. Buxton, C.L. Greenstock, W.P. Helman, A.B. Ross, Critical review of rate constants for reactions of hydrated electrons, hydrogen atoms and hydroxyl radicals (·OH/·O− in aqueous solution, J. Phys. Chem. Ref. Data 17 (1988) 513–886, https://doi.org/10.1063/1.555805.

[71] N.I. Kuznetsova, N.V. Kirillova, L.I. Kuznetsova, M.Y. Smirnova, V.A. Likholobov, Hydrogen peroxide and oxygen–hydrogen oxidation of aromatic compounds in catalytic systems containing heteropoly compounds, J. Hazard. Mater. 146 (2007) 569–576, https://doi.org/10.1016/j.jhazmat.2007.04.058.

[72] G. Strukul, Catalytic oxidations with hydrogen peroxide as oxidant, 1992. https://doi.org/10.1007/978-94-017-0984-2.

[73] B.H.J. Bielski, D.E. Cabelli, R.L. Arudi, A.B. Ross, Reactivity of HO2/O−2 radicals in aqueous solution, J. Phys. Chem. Ref. Data 14 (1985) 1041–1100, https://doi.org/10.1063/1.555739.

[74] C. Bai, W. Xiao, D. Feng, M. Xian, D. Guo, Z. Ge, Y. Zhou, Efficient decolorization of Malachite green in the Fenton reaction catalyzed by [Fe(III)-salen]Cl complex, Chem. Eng. J. 215–216 (2013) 227–234, https://doi.org/10.1016/j.cej.2012.09.124.

[75] M.E.Samar A.Balaska, A. Grid, Phenol photodegradation process assisted with Wells–Dawson heteropolyacids, Desalin. Water Treat. 54 (2014) 382–392, https://doi.org/10.1080/19443994.2014.883577.

[76] H.-J. Fan, S.-T. Huang, W.-H. Chung, J.-L. Jan, W.-Y. Lin, C.-C. Chen, Degradation pathways of crystal violet by Fenton and Fenton-like systems: condition optimization and intermediate separation and identification, J. Hazard. Mater. 171 (2009) 1032–1044, https://doi.org/10.1016/j.jhazmat.2009.06.117.

[77] Y. Sha, I. Mathew, Q. Cui, M. Clay, F. Gao, X.J. Zhang, Z. Gu, Rapid degradation of azo dye methyl orange using hollow cobalt nanoparticles, Chemosphere 144 (2016) 1530–1535, https://doi.org/10.1016/j.chemosphere.2015.10.040.

[78] Z.M. Abou-Gamra, Kinetic and thermodynamic study for fenton-like oxidation of amaranth red dye, Adv. Chem. Eng. Sci. 04 (2014) 285–291, https://doi.org/10.4236/aces.2014.43031.

[79] E.Gkika A.Troupis, T. Triantis, A. Hiskia, E. Papaconstantinou, Photocatalytic reductive destruction of azo dyes by polyoxometallates: naphthol blue black, J. Photochem. Photobiol. Chem. 188 (2007) 272–278, https://doi.org/10.1016/j.jphotochem.2006.12.022.

[80] Z. Mengyue, C. Shifu, T. Yaowu, Photocatalytic degradation of organophosphorus pesticides using thin films of TiO2, J. Chem. Technol. Biotechnol. 64 (1995) 339–344, https://doi.org/10.1002/jctb.280640405.

[81] O. Moradi, M.A. Madanpisheh, M. Moghaddas, Synthesis of GO/HEMA, GO/HEMA/TiO2, and GO/Fe3O4/HEMA as novel nanocomposites and their dye removal ability, Adv. Compos. Hybrid Mater. 4 (2021) 1185–1204, https://doi.org/10.1007/s42114-021-00353-7.

[82] B.H. Hameed, T.W. Lee, Degradation of malachite green in aqueous solution by Fenton process, J. Hazard. Mater. 164 (2009) 468–472, https://doi.org/10.1016/j.jhazmat.2008.08.018.

[83] Z. Shams-Ghahfarokhi, A. Nezamzadeh-Ejhieh, As-synthesized ZSM-5 zeolite as a suitable support for increasing the photoactivity of semiconductors in a typical photodegradation process, Mater. Sci. Semicond. Process. 39 (2015) 265–275, https://doi.org/10.1016/j.mssp.2015.05.022.

[84] U. Hübner, S. Spahr, H. Lutze, A. Wieland, S. Rüting, W. Gernjak, J. Wenk, Advanced oxidation processes for water and wastewater treatment – guidance for systematic future research, Heliyon (2024) e30402, https://doi.org/10.1016/j.heliyon.2024.e30402.

[85] A. Shojaei, A. Rezvani, M. Heravi, A green, reusable and highly efficient solid acid catalyst for the oxidation of aldehydes to the corresponding carboxylic acids using H2O2 and KMnO4: H5PV2Mo10O40 (10-molybdo-2-vanadophosphoric heteropolyacid), J. Serb. Chem. Soc. 76 (2011) 1513–1522, https://doi.org/10.2298/jsc100920135s.

[86] S. Qourzal, M. Tamimi, A. Assabbane, Y. Ait-Ichou, influence de certains ions inorganiques, de l'éthanol et du peroxyde d'hydrogène sur la photominéralisation du β-naphtol en présence de TiO2, C.R. Chim. 10 (2007) 1187–1194, https://doi.org/10.1016/j.crci.2007.06.011.

[87] M. Brigante, M. Minella, G. Mailhot, V. Maurino, C. Minero, D. Vione, Formation and reactivity of the dichloride radical (Cl2-) in surface waters: A modelling approach, Chemosphere 95 (2014) 464–469, https://doi.org/10.1016/j.chemosphere.2013.09.098.

[88] R. Yuan, S.N. Ramjaun, Z. Wang, J. Liu, Effects of chloride ion on degradation of Acid Orange 7 by sulfate radical-based advanced oxidation process: implications for formation of chlorinated aromatic compounds, J. Hazard. Mater. 196 (2011) 173–179, https://doi.org/10.1016/j.jhazmat.2011.09.007.

[89] G.K.C. Low, S.R. McEvoy, R.W. Matthews, Formation of nitrate and ammonium ions in titanium dioxide mediated photocatalytic degradation of organic compounds containing nitrogen atoms, Environ. Sci. Technol. 25 (1991) 460–467, https://doi.org/10.1021/es00015a013.

[90] M. Kositzi, A. Antoniadis, I. Poulios, I. Kiridis, S. Malato, Solar photocatalytic treatment of simulated dyestuff effluents, Sol. Energy 77 (2004) 591–600, https://doi.org/10.1016/j.solener.2004.04.018.

[91] A. Zaouak, A. Noomen, H. Jelassi, Gamma-radiation induced decolorization and degradation on aqueous solutions of Indigo Carmine dye, J. Radioanal. Nucl. Chem. 317 (2018) 37–44, https://doi.org/10.1007/s10967-018-5835-z.

[92] J. Han, H.-Y. Zeng, S. Xu, C.-R. Chen, X.-J. Liu, Catalytic properties of CuMgAlO catalyst and degradation mechanism in CWPO of methyl orange, Appl. Catal. General 527 (2016) 72–80, https://doi.org/10.1016/j.apcata.2016.08.015.

[93] M. Moudjahed, L. Dermeche, S. Benadji, T. Mazari, C. Rabia, Dawson-type polyoxometalates as green catalysts for adipic acid synthesis, J. Molec. Catal. Chem. 414 (2016) 72–77, https://doi.org/10.1016/j.molcata.2015.12.014.

[94] A. Sudha, N. Anuradha, M. Baneto, K. Ravichandran, M. Varshini, M. Ayyanar, M. S.A. Raj, I. Manimehan, Role of g-C3N4 as a 2-D composite partner in enhancing the photocatalytic waste water detoxifying ability of green routed cerium doped zinc oxide, J. Mol. Struct. 1325 (2024) 141013, https://doi.org/10.1016/j.molstruc.2024.141013.

[95] I.Manimehan A.Sudha, M. Baneto, M. Varshini, K. Ravichandran, M. Ayyanar, B. Sundaresan, S. Jeya, Influence of simultaneous cationic and anionic doping, and composite partnering on the photocatalytic dye detoxification ability of green synthesized ZnO: W:F/g-C3N4 nanocomposite, Emergent Mater. (2024) 1–14, https://doi.org/10.1007/s42247-024-00848-1.

[96] R. Sumethra, T. Jayakumari, N. Anuradha, K. Ravichandran, M. Varshini, M. Ayyanar, P.K. Praseetha, Effect of nanocomposite partnering of g-C3N4 with Morinda pubescens leaf extract mediated Sr doped Ni/NiO on the photocatalytic dye detoxification: confirmation by seed germination test, Diamond Relat. Mater. 150 (2024) 111716, https://doi.org/10.1016/j.diamond.2024.111716.

[97] M. Varshini, K. Ravichandran, M. Ayyanar, R. Anandhi, R. Manimekalai, Effective dye detoxification by Cassia fistula flower extract- powered photocatalytic nanocomposite, SnO2:Mo/rGO and phytotoxicity evaluation of treated water using cowpea seeds, J. Environ. Chem. Eng. 12 (2024) 113270, https://doi.org/10.1016/j.jece.2024.113270.

[98] L. Li, P. Ma, J. Wang, J. Niu, A new inorganic 2D network polyoxometalate constructed from Wells–Dawson phosphomolybdate linked through Cu(II) ions, Inorg. Chem. Commun. 34 (2013) 23–26, https://doi.org/10.1016/j.inoche.2013.04.007.